
INVERTING SELF-ORGANIZING MAPS: A UNIFIED ACTIVATION-BASED FRAMEWORK

Alessandro Londei

Sony Computer Science Laboratories - Rome
Joint Initiative CREF-SONY, Centro Ricerche Enrico Fermi
Via Panisperna 89/A, 00184
Rome, Italy
alessandro.londei@sony.com

Matteo Benati

Department of Computer, Automatic and Management Engineering
Sapienza University, Via Ariosto 25
Rome, Italy
matteo.benati@uniroma1.it

Denise Lanzieri

Sony Computer Science Laboratories - Rome
Joint Initiative CREF-SONY, Centro Ricerche Enrico Fermi
Via Panisperna 89/A, 00184
Rome, Italy
denise.lanzieri@sony.com

Vittorio Loreto

Sony Computer Science Laboratories - Rome
Joint Initiative CREF-SONY, Centro Ricerche Enrico Fermi
Via Panisperna 89/A, 00184
Rome, Italy
Physics Department
Sapienza University, Piazzale Aldo Moro 1
Rome, Italy
Complexity Science Hub
Josefstädter Strasse 39, A 1080, Vienna, Austria
vittorio.loreto@sony.com

ABSTRACT

Self-Organizing Maps (SOMs) provide topology-preserving projections of high-dimensional data, yet their use as generative models remains largely unexplored. We show that the activation pattern of a SOM—the squared distances to its prototypes—can be *inverted* to recover the exact input, following from a classical result in Euclidean distance geometry: a point in D dimensions is uniquely determined by its distances to $D+1$ affinely independent references. We derive the corresponding linear system and characterize the conditions under which inversion is well-posed. Building on this mechanism, we introduce the *Manifold-Aware Unified SOM Inversion and Control* (MUSIC) update rule, which modifies squared distances to selected prototypes while preserving others, producing controlled, semantically meaningful trajectories aligned with the SOM’s piecewise-linear structure. Tikhonov regularization stabilizes the update and ensures smooth motion in high dimensions. Unlike variational or diffusion-based generative models, MUSIC requires no sampling, latent priors, or

learned decoders: it operates entirely on prototype geometry. If no perturbation is applied, inversion recovers the exact input; when a target prototype or cluster is specified, MUSIC produces coherent semantic transitions. We validate the framework on synthetic Gaussian mixtures, MNIST digits, and the Labeled Faces in the Wild dataset. Across all settings, MUSIC trajectories maintain high classifier confidence, produce significantly sharper intermediate images than linear interpolation, and reveal an interpretable geometric structure of the learned map.

Keywords Self-Organizing Maps · Activation inversion · Topology-preserving generation · Latent space navigation · Tikhonov regularization

1 Introduction

Self-Organizing Maps (SOMs) [1, 2] are classical topology-preserving neural models that embed high-dimensional data into a structured two-dimensional lattice of prototype vectors. Through competitive learning and neighbourhood cooperation, a SOM organizes prototypes so that nearby units respond to similar inputs, providing an interpretable low-dimensional representation of the data manifold. This property has made SOMs influential in applications ranging from image analysis [3] and speech processing [4] to genomics [5] and exploratory visualization [6]. Over the years, several architectural variants—such as Growing Neural Gas [7], Dynamic SOMs [8], hierarchical maps [9], and prototype-regularized deep models like SOM-VAE [10]—have extended the expressive power of SOM-based learning while preserving its foundation in prototype geometry.

Traditionally, SOMs are used as a form of structured vector quantization: each input $z \in \mathbb{R}^D$ is associated with its Best-Matching Unit (BMU), and the BMU index serves as a discrete representation of the data. In this work, we adopt a fundamentally different viewpoint. Rather than mapping data *to* prototypes, we show that the SOM activation pattern—specifically, the squared distances from z to all prototypes—contains enough geometric information to *reconstruct* z exactly (Section 2).

Building on this observation, we introduce a unified geometric framework for continuous semantic transformations in the data space. Our method proceeds in three steps:

1. **Exact inversion.** From the squared-distance activations to the prototypes, solve a linear system to recover the input vector z . When the SOM prototypes span \mathbb{R}^D , inversion is exact up to machine precision.
2. **Structured perturbation of activations.** Selectively modify the squared distances to a chosen subset of prototypes (e.g., a target cluster or a single prototype) while preserving the others. These perturbations must satisfy Euclidean realizability constraints, which we enforce via a Tikhonov-regularized linear system.
3. **MUSIC update rule.** The resulting *Manifold-Aware Unified SOM Inversion and Control* (MUSIC) update produces a latent step Δz that simultaneously moves toward the desired prototypes while maintaining consistency with the preserved distances.

This framework turns a SOM from a static discretizer into a continuous, interpretable mechanism for latent-space exploration. In contrast to generative models that rely on learned decoders and latent priors [11, 12, 13], MUSIC operates entirely on prototype geometry. If no conditioning is applied, inversion reproduces the exact input; when conditioning is introduced, MUSIC yields semantically meaningful variations that remain on the manifold encoded by the SOM.

We validate the method across datasets of increasing complexity: synthetic Gaussian mixtures (where ground truth geometry is known), handwritten digits (MNIST), and natural face images (Labeled Faces in the Wild). Across all settings, MUSIC generates coherent semantic trajectories that maintain high classifier confidence, produce significantly sharper intermediate images than linear interpolation, and preserve local identity where appropriate.

The contributions of this paper are therefore twofold: (i) showing that classical SOM activations admit exact inversion through distance geometry, and (ii) introducing a principled update rule that turns the SOM into a geometry-aware engine for semantic latent-space navigation.

2 Inverting Self-Organizing Maps

Let $\{w_j\}_{j=1}^N \subset \mathbb{R}^D$ denote the prototype (weight) vectors of a trained SOM. For any input vector $z \in \mathbb{R}^D$, define the *squared-distance activation vector*

$$a(z) = \begin{bmatrix} a_1(z) \\ \vdots \\ a_N(z) \end{bmatrix}, \quad a_j(z) = \|z - w_j\|^2.$$

We work with *squared* distances because $a_j(z)$ has linear first-order variation, $da_j = 2(z - w_j)^\top dz$, yielding a well-conditioned local Jacobian. Moreover, subtracting any reference activation $a_r(z)$ removes the common quadratic term $\|z\|^2$, exposing an *affine* dependence on z that is crucial for exact inversion. The mapping $f : \mathbb{R}^D \rightarrow \mathbb{R}^N$, $f(z) = a(z)$, can be interpreted as the activation state of the SOM when exposed to z . Recovering z from its distances to a sufficiently rich set of references is a standard consequence of Euclidean distance geometry and multilateration [14, 15, 16, 17]. The activations are moreover invariant under rigid motions of the prototype set (Appendix S1.1), so only the relative configuration of prototypes matters for inversion.

2.1 Exact Inversion Property

The following proposition establishes that f is injective and exactly invertible under a mild rank condition on the prototypes.

Proposition 1 (Exact Inversion Property). *If the prototype set $\{w_j\}_{j=1}^N$ spans \mathbb{R}^D , i.e. $\text{rank}([w_1 - w_N, \dots, w_{N-1} - w_N]) = D$, then the mapping f is injective. Moreover, the input vector z can be exactly reconstructed from the activation differences $\{a_j(z) - a_N(z)\}_{j=1}^{N-1}$ by solving a linear system:*

$$z = (B^\top B)^{-1} B^\top c,$$

where

$$B = \begin{bmatrix} 2(w_N - w_1)^\top \\ \vdots \\ 2(w_N - w_{N-1})^\top \end{bmatrix} \in \mathbb{R}^{(N-1) \times D}, \quad c = \begin{bmatrix} a_1(z) - a_N(z) + \|w_N\|^2 - \|w_1\|^2 \\ \vdots \\ a_{N-1}(z) - a_N(z) + \|w_N\|^2 - \|w_{N-1}\|^2 \end{bmatrix}.$$

Proof. Each squared activation expands as $a_j(z) = z^\top z - 2z^\top w_j + \|w_j\|^2$. Subtracting $a_N(z)$ eliminates the quadratic term:

$$a_j(z) - a_N(z) = 2(w_N - w_j)^\top z + \|w_j\|^2 - \|w_N\|^2, \quad j = 1, \dots, N-1.$$

This defines an affine system $Bz = c$ with B and c as above. If B has full column rank D , the Moore–Penrose pseudoinverse gives

$$z = B^+ c = (B^\top B)^{-1} B^\top c, \tag{1}$$

and the reconstruction is exact. \square

The reference index N is arbitrary: any anchor $r \in \{1, \dots, N\}$ yields an equivalent system. In practice, centering the prototypes and optionally whitening can improve the conditioning of B . This linearization connects to classical Euclidean distance geometry: activation differences form an affine slice of a Euclidean Distance Matrix (EDM), whose embedding is unique up to rigid motions under mild rank conditions [14, 15, 18].

2.2 Stability and Conditioning

Corollary 1 (Stability to activation noise). *Let $\tilde{a}_j(z) = a_j(z) + \varepsilon_j$ with $\varepsilon \sim \mathcal{N}(0, \sigma^2 I)$. If B has full column rank, the least-squares inverse satisfies*

$$\|\hat{z} - z\| \leq \|B^+\| \sigma \sqrt{N-1}.$$

Hence, inversion is Lipschitz-stable, with amplification governed by the inverse of the smallest singular value of B .

Figure 1 empirically validates this bound: across 20,000 noisy trials, the reconstruction error $\|z - \hat{z}\|_2$ grows as $\sigma_{\min}(B)$ decreases, following the predicted scaling

$$\mathbb{E} \|\hat{z} - z\|_2^2 = \sigma^2 \text{tr}((B^\top B)^{-1}) \lesssim \sigma^2 \frac{D}{\sigma_{\min}^2(B)}.$$

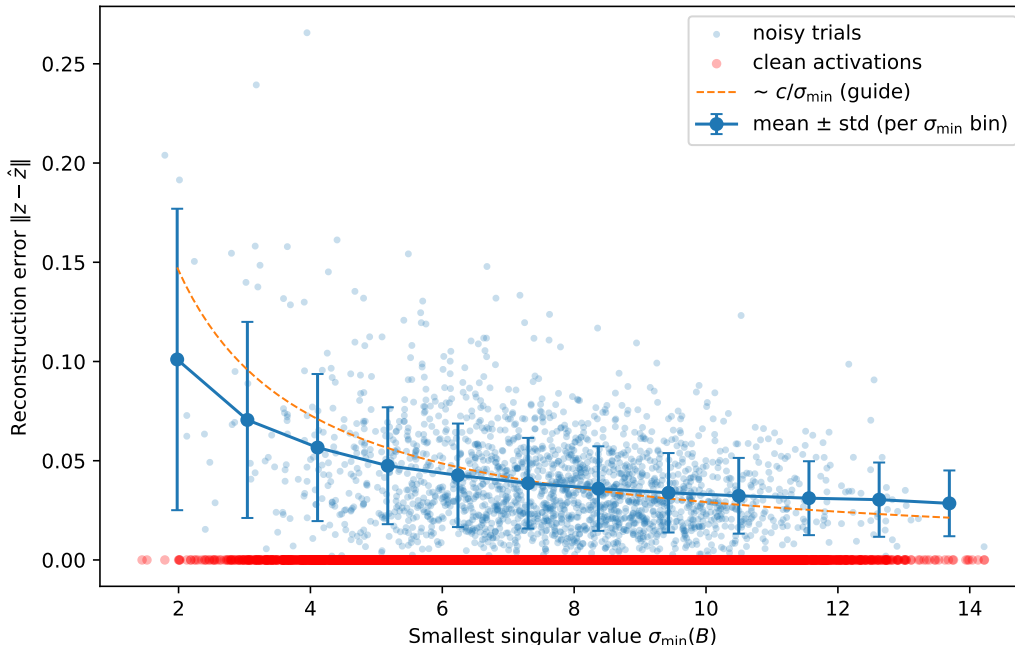


Figure 1: **Inversion accuracy vs. conditioning of the prototype geometry.** Clean activations (red) yield reconstructions at machine precision. Adding Gaussian noise induces errors that grow as $1/\sigma_{\min}(B)$: well-spread prototypes give stable inversion, while better collinear configurations amplify noise. Blue circles show binned means \pm standard deviations over 20,000 trials.

For overcomplete maps ($N > D+1$), the system is consistent and inversion reduces to least squares, with reconstruction errors at double-precision level ($\sim 10^{-18}$). A weighted least-squares extension for correlated noise is given in Appendix S1.3.

When the ambient dimension exceeds the rank of the prototype matrix (e.g., raw pixel inputs), dimensionality reduction (PCA or an autoencoder bottleneck) is necessary before inversion can succeed. The Jacobian $J(z) \in \mathbb{R}^{N \times D}$ with rows $J_j(z) = 2(z - w_j)^\top$ has full rank D for all $z \in \mathbb{R}^D$ whenever the prototypes contain $D+1$ affinely independent points (Appendix S1.2); we use this in the perturbation analysis of Section 3.

This exact-inversion property establishes the SOM activation map as a mathematically well-posed latent representation. In the next section, we exploit it to define small, consistent perturbations in activation space that translate into interpretable input-space variations.

3 Perturbing the SOM activation layer

Having established that the activation map admits exact inversion, we now use it as a control interface. We perturb distances to selected prototypes and recover the corresponding latent update by solving a regularized inverse problem, yielding smooth and semantically meaningful variations of z .

We denote by $\text{BMU}(z) = \arg \min_j \|z - w_j\|$ the best-matching unit and by \mathcal{V}_j its Voronoi region [19]. The collection $\{\mathcal{V}_j\}$ forms a Voronoi tessellation of the input space, providing the piecewise-linear partition underlying the SOM topology. Each input $z \in \mathbb{R}^D$ induces an activation pattern $a(z) = \{\|z - w_j\|^2\}_{j=1}^N$; small, geometrically consistent perturbations of this pattern yield coherent variations of z , provided the modified activations remain compatible with a valid Euclidean configuration. Arbitrary changes of individual activations generally violate this consistency, as all prototype distances are mutually dependent [19, 20, 21]. Figure 2 illustrates this geometric interdependence for a perturbation applied to a single prototype.

To introduce a valid perturbation, we seek the smallest change $\Delta z \in \mathbb{R}^D$ that produces a prescribed modification in the distance to a selected prototype while approximately preserving the geometry of the other distances. Let

$$z \in \mathbb{R}^D, \quad \{w_j\}_{j=1}^N \subset \mathbb{R}^D, \quad k \in \{1, \dots, N\}, \quad \Delta d_k \in \mathbb{R},$$

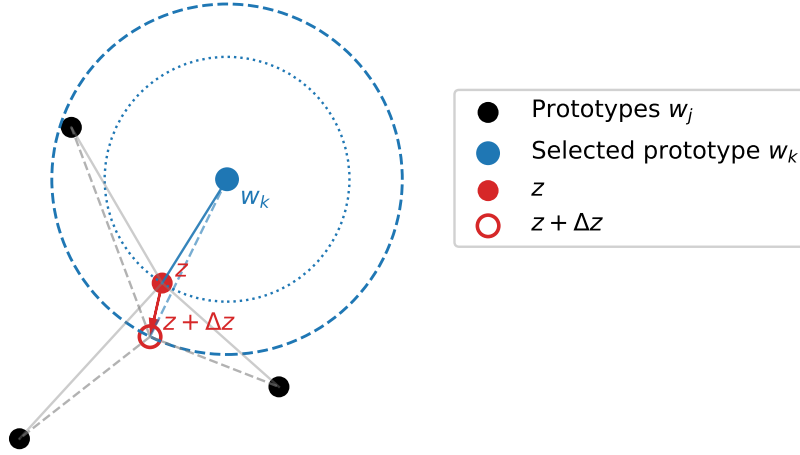


Figure 2: **Geometric schematic of a single-cell perturbation in the SOM activation space.** A small displacement Δz of the input vector z modifies its distance to the selected prototype w_k , thereby inducing a consistent reconfiguration of distances to all other prototypes w_j . Solid lines indicate the original distances $\|z - w_j\|$, and dashed lines the updated distances $\|z + \Delta z - w_j\|$. Because all distances are mutually constrained by the geometry of \mathbb{R}^D , a perturbation of one activation cell necessarily entails a coordinated adaptation of the others to maintain a valid Euclidean configuration.

where w_j are the prototype vectors and Δd_k is the desired increment in the distance between z and w_k . The goal is to determine a perturbation vector Δz satisfying:

1. the distance to prototype k changes by Δd_k ;
2. the norm $\|\Delta z\|$ is minimal (scaled by a user-defined parameter r_{scale});
3. the relative geometry of all other distances is approximately preserved.

Defining the relative position and current distance

$$x := z - w_k, \quad d_k := \|x\|, \quad d'_k := d_k + \Delta d_k,$$

the desired squared change in distance is

$$\Delta d_k^2 = (d'_k)^2 - d_k^2 = \|x + \Delta z\|^2 - \|x\|^2.$$

Expanding gives

$$\|x + \Delta z\|^2 = \|x\|^2 + 2x^\top \Delta z + \|\Delta z\|^2,$$

and thus

$$2x^\top \Delta z + \|\Delta z\|^2 = \Delta d_k^2.$$

For infinitesimal perturbations, the quadratic term is second-order and can be neglected, yielding the first-order constraint:

$$x^\top \Delta z = c := \frac{1}{2} \Delta d_k^2.$$

This fixes the projection of Δz along x . Decomposing the perturbation as

$$\Delta z = \Delta z_{\parallel} + \Delta z_{\perp}, \quad \Delta z_{\parallel} = \frac{c}{\|x\|^2} x, \quad x^\top \Delta z_{\perp} = 0,$$

one obtains a parallel component that achieves the desired change in distance and an orthogonal component spanning the local isodistance subspace. Geometrically, Δz_{\perp} belongs to the tangent space of the SOM distance manifold: in the linear regime, such directions leave all squared distances approximately unchanged to first order. Crucially, in high dimensions, tangential perturbations become increasingly close to true isometries: the first-order distance variations satisfy $|\Delta a_j| \sim \|\Delta z_{\perp}\| \|c_j\| / \sqrt{D}$ (where $c_j = w_k - w_j$), so that the relative distortion of non-target distances vanishes as D grows, while the $O(\|\Delta z\|^2)$ remainder of the Taylor expansion controls the ultimate accuracy of the linear approximation. A formal derivation of this concentration effect is given in Supplementary Section S2.

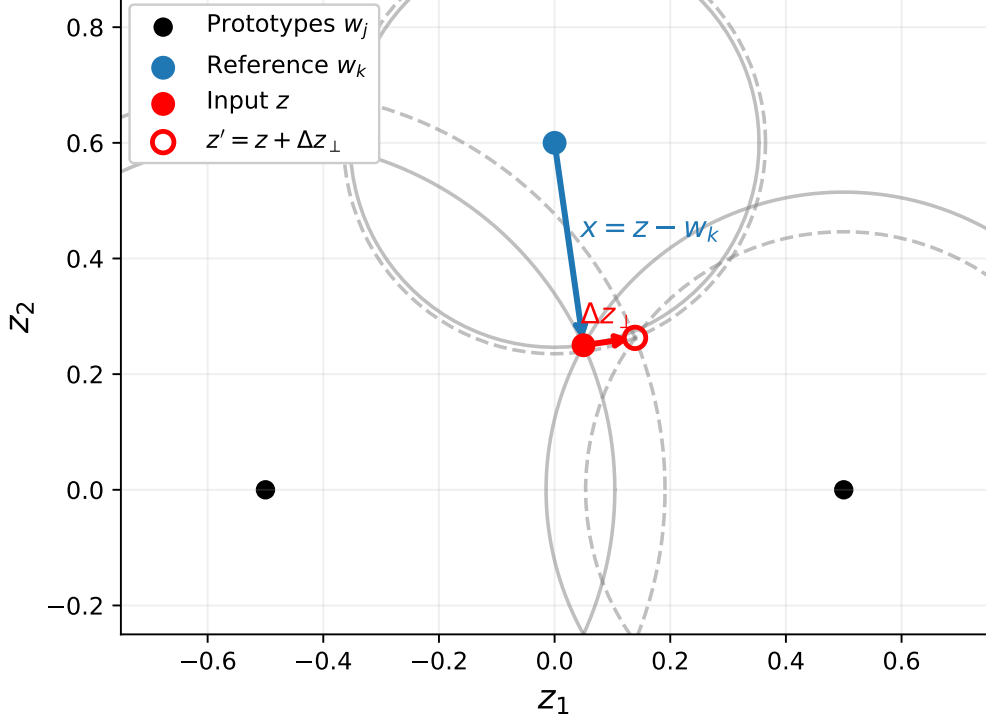


Figure 3: **Radial-tangential decomposition around a reference prototype.** Black dots denote the SOM prototypes w_j , and the blue point marks the reference prototype w_k . The red point shows the current input z , while the unfilled red point indicates the tangentially displaced location $z' = z + \Delta z_{\perp}$. The blue arrow represents the radial direction $x = z - w_k$, which determines the first-order change of the squared distance to the reference prototype. The red arrow shows a tangential perturbation Δz_{\perp} orthogonal to x at z . For each prototype, the solid circle traces the locus of points at the same distance as z , while the dashed circle shows the corresponding locus for z' . The circles centered at w_k coincide at first order, and the circles centered at the other prototypes remain nearly unchanged in the neighborhood of z , illustrating that tangential motion approximately preserves all squared distances simultaneously.

Importantly, the accuracy of this linearisation can be characterised exactly for squared-distance activations. Since each $a_j(z) = \|z - c_j\|^2$ is quadratic in z , its Taylor expansion terminates at second order:

$$a_j(z + \Delta z) = a_j(z) - 2(c_j - z)^{\top} \Delta z + \|\Delta z\|^2.$$

The second-order residual $\|\Delta z\|^2$ is independent of j : it shifts all activations by the same amount. In the anchored system used throughout this work, which operates on activation *differences* $a_j - a_r$ relative to a reference prototype r , this common term cancels exactly, leaving

$$(a_j - a_r)(z + \Delta z) - (a_j - a_r)(z) = -2(c_j - c_r)^{\top} \Delta z,$$

which is linear in Δz with a constant coefficient matrix. The first-order Jacobian model is therefore not an approximation but the exact relationship for activation differences under squared-distance activations. In absolute terms, the sole residual is the uniform bias $\|\Delta z\|^2 = O(\rho^2)$, which does not affect the direction of the optimal update, only its magnitude.

In absolute (non-anchored) terms, the sole residual is the uniform bias $\|\Delta z\|^2$, which is $O(\rho^2)$ under the step-size clipping enforced in MUSIC and does not affect the *direction* of the optimal update Δz , only its magnitude. This structural property of quadratic activations is what distinguishes the MUSIC linearisation from generic Taylor approximations, where both the magnitude and direction of the remainder depend on the nonlinear form of the activation function and can accumulate unpredictably.

A geometric illustration of the radial–tangential decomposition and its effect on all SOM prototypes is provided in Figure 3.

To control amplitude, we set a total perturbation norm $r := r_{\text{scale}} \|\Delta z\|$ and assign

$$\|\Delta z_{\perp}\| = \sqrt{r^2 - \|\Delta z_{\parallel}\|^2}.$$

The resulting perturbation combines a controlled radial shift with a tangential adjustment that minimally disturbs the remaining distances.

The image $\mathcal{A} = \{a(z) : z \in \mathbb{R}^D\} \subset \mathbb{R}^N$ forms a smooth D -dimensional submanifold of activation space. By the full-rank Jacobian property (Appendix S1.2), the tangent space at each point is $T_{a(z)}\mathcal{A} = \text{Im } J(z)$ with $J_j(z) = 2(z - w_j)^\top$. Any activation vector $\tilde{a} \notin \mathcal{A}$ violates the consistency relations

$$a_i(z) - a_j(z) = 2(w_j - w_i)^\top z + \|w_i\|^2 - \|w_j\|^2$$

and cannot correspond to a valid point in \mathbb{R}^D . Perturbing a single activation in isolation therefore moves $a(z)$ off \mathcal{A} ; to recover a consistent state, the modified activation must be reprojected by solving

$$\hat{z} = \arg \min_{z \in \mathbb{R}^D} \|a(z) - \tilde{a}\|^2.$$

This motivates the MUSIC framework (Section 4), which casts multi-prototype activation perturbations as the solution of a Tikhonov-regularized inverse problem balancing target attraction and global geometry preservation.

4 The MUSIC framework

Building on the geometric constraints of the previous section, we now seek a principled way to steer the SOM activation state while preserving the consistency of its distance representation. A single-cell perturbation (Section 3) can be analytically described, but extending this to multiple prototypes or continuous trajectories requires a unified formulation [22].

We introduce the *Manifold-Aware Unified SOM Inversion and Control* (MUSIC) framework, in which all activation-based perturbations are expressed as Tikhonov-regularized inverse problems. Given a desired change in one or more prototype activations, MUSIC computes the minimal, geometrically consistent perturbation of the input vector, balancing three objectives: (i) preservation of non-target activations, (ii) attraction toward the desired activation changes, and (iii) regularization for smoothness and numerical stability. The resulting update admits a closed-form solution, interpretable both as a weighted projection in input space and as the MAP estimate of a Gaussian model (Appendix S5).

4.1 Energy formulation and update rule

MUSIC computes at each iteration a perturbation $\Delta z \in \mathbb{R}^D$ that realizes a desired change in squared-distance activations while preserving the remaining geometry. Let $a_j(z) = \|z - w_j\|^2$ with Jacobian row $J_j(z) = 2(z - w_j)^\top$. Given a preserved index set S and a target set T , we form A_S and B_T by stacking the (optionally row-normalized) Jacobian rows $\{\hat{J}_j\}_{j \in S}$ and $\{\hat{J}_t\}_{t \in T}$, evaluated at the current iterate z_t (see Appendix S6 for row-normalization details).

MUSIC chooses Δz as the minimizer of the Tikhonov-regularized energy (Appendix S3 derives the full functional):

$$E_\gamma(\Delta z) = (1 - \gamma) \|A_S \Delta z\|^2 + \gamma \|B_T \Delta z - b\|^2 + \lambda \|\Delta z\|^2, \quad \gamma \in [0, 1], \lambda > 0, \quad (2)$$

where b encodes the desired first-order target changes (e.g., $b_t = \frac{1}{2} \Delta a_t$). The normal equations are

$$\left[(1 - \gamma) A_S^\top A_S + \gamma B_T^\top B_T + \lambda I \right] \Delta z^* = \gamma B_T^\top b. \quad (3)$$

With $H = (1 - \gamma) A_S^\top A_S + \gamma B_T^\top B_T + \lambda I \succ 0$ (positive definite for any $\lambda > 0$), the unique minimizer is $\Delta z^* = H^{-1} \gamma B_T^\top b$. Geometrically, $\lambda \|\Delta z\|^2$ induces an isotropic trust region in the tangent space, damping motion in poorly supported directions. In practice we enforce a step constraint $\|\Delta z^*\| \leq \rho$ and relinearize A_S, B_T at $z_{t+1} = z_t + \Delta z^*$ to maintain first-order accuracy.

The Tikhonov parameter λ acts as a spectral low-pass filter on the combined constraint system: directions with small singular values (ill-conditioned or conflicting constraints) are attenuated, while well-supported modes pass nearly unaltered. A detailed spectral analysis with filtering bounds is given in Appendix S4.

Iterating the update yields a discrete trajectory that, in the small-step limit, follows the regularized gradient flow $\dot{z} = -\nabla_z E_\gamma(z)$, connecting the inverse-problem formulation to Riemannian gradient dynamics on the SOM distance manifold [23, 24].

In practice, MUSIC does not enforce exact isometries. Each step balances modifying the target distances with approximately preserving the complement, using the tangent-space geometry of Section 3 to bias the evolution toward manifold-consistent, semantically meaningful changes. The preservation set S may include all non-targets or an r -ring lattice neighborhood around the current BMU. Empirically stable trajectories are obtained with $\gamma \in [0.7, 0.95]$, λ chosen via the L-curve criterion [25], and a trust radius $\rho = 0.02 \|z - w_{\text{BMU}}\|$.

4.2 Exploration modes: free, informed, and cluster

The MUSIC energy (2) specializes to three regimes by choosing the sets (S, T) and the target vector b . In all cases we work with the linearized operators at z_t :

$$J_j(z_t) = 2(z_t - w_j)^\top, \quad A_S = \text{stack}\{\hat{J}_j : j \in S\}, \quad B_T = \text{stack}\{\hat{J}_t : t \in T\},$$

with optional diagonal weights W_S, W_T to emphasize local topology. Step-by-step pseudo-code for all three modes, including noise injection for enhanced coverage, is given in Appendix S8.

(i) Free exploration (no explicit target)

Free exploration seeks geometry-preserving motion without attraction toward any prototype: a local random walk on the activation manifold. Removing the target term in (2) ($B_T = 0$, b omitted) yields

$$\min_{\Delta z} \|W_S A_S \Delta z\|^2 + \lambda \|\Delta z\|^2 \quad \text{s.t.} \quad \|\Delta z\| \leq \tau. \quad (4)$$

The trivial minimizer is $\Delta z = 0$; one therefore selects a direction in which preserved activations change minimally. Let $C = (W_S A_S)^\top (W_S A_S) + \lambda I$. Any unit eigenvector q_{\min} of the smallest eigenvalue of C identifies the least disruptive direction, giving $\Delta z^* = \tau q_{\min}$. Stochastic exploration is obtained by sampling from the low-eigenvalue subspace of C , optionally adding a small radial component toward the current BMU to avoid drift.

(ii) Informed exploration (single target)

Informed exploration moves the input toward a chosen prototype t while preserving non-target distances. Let $T = \{t\}$, $S = \{1, \dots, N\} \setminus \{t\}$, and set

$$B_T = \hat{J}_t, \quad b = -\eta a_t(z_t) \quad (\eta \in (0, 1]),$$

requesting a fractional reduction of the target activation. The MUSIC step solves

$$\min_{\Delta z} \|W_S A_S \Delta z\|^2 + \gamma \|W_T (B_T \Delta z - b)\|^2 + \lambda \|\Delta z\|^2. \quad (5)$$

This single-target variant recovers the radial/tangential decomposition of Section 3 in the limit of vanishing λ , while providing a numerically stable, one-shot update integrating preservation and attraction under a single convex objective.

(iii) Cluster exploration (multi-target)

Cluster exploration generalizes to coordinated motion toward a group of related prototypes T , preserving distances to the complement $S = \{1, \dots, N\} \setminus T$. We solve

$$\min_{\Delta z} \underbrace{\|W_S A_S \Delta z\|^2}_{\text{preserve non-targets}} + \gamma \underbrace{\|W_T (B_T \Delta z - b)\|^2}_{\text{shrink targets}} + \lambda \|\Delta z\|^2, \quad (6)$$

with $b_t = -\eta a_t(z_t)$ for each $t \in T$. Writing $A_w = W_S A_S$, $B_w = \sqrt{\gamma} W_T B_T$, and $b_w = \sqrt{\gamma} W_T b$, the normal equations are

$$(A_w^\top A_w + B_w^\top B_w + \lambda I) \Delta z^* = B_w^\top b_w. \quad (7)$$

We update $z_{t+1} = z_t + \Delta z^*$, enforce the trust radius, and relinearize; $m = 1\text{--}3$ passes typically suffice. When T is large, Gaussian weights in W_T emphasize nearby targets and improve conditioning.

A lighter variant, *random informed-within-cluster* exploration, draws a single prototype $t^{(i)} \sim \text{Uniform}(T)$ at each step and applies the informed update toward $t^{(i)}$ alone. In expectation this approximates the full multi-target control while reducing per-step cost, and empirically improves mixing by avoiding bias toward the cluster barycenter.

All three regimes share the same convex backbone and differ only in (S, T, b) . In practice we solve the normal equations via Cholesky factorization (moderate D) or conjugate gradients (large D), increase λ or taper W_S, W_T if conditioning deteriorates, and relinearize after each step to maintain first-order accuracy.

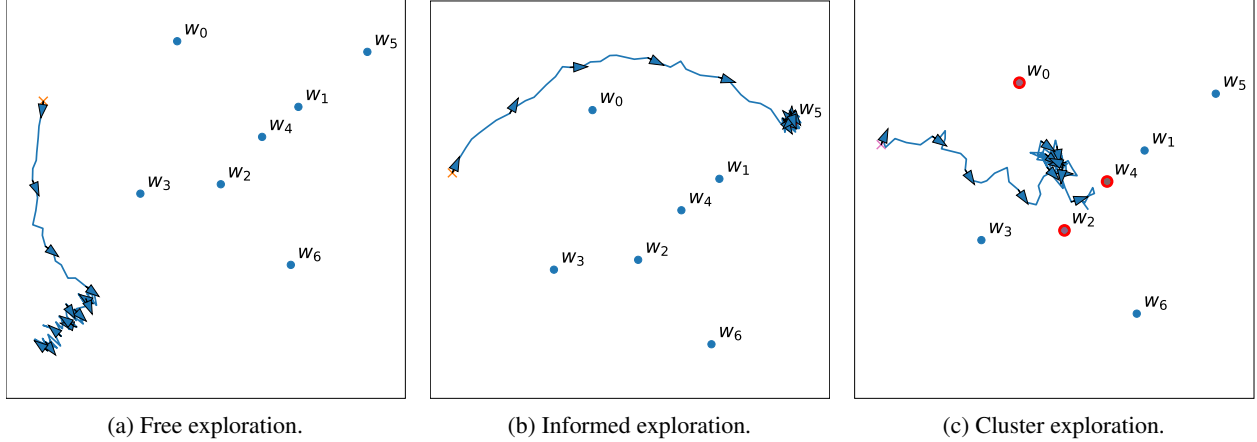


Figure 4: **Exploration modes with consistent activation editing (2D toy)**. Seven prototypes (dots) are placed in $[-2.5, 2.5]^2$; all trajectories start from the same z_0 (cross). (a) Free: the update follows the least-perturbing eigenvector of $J(z)^\top J(z)$, producing gentle drift. (b) Informed: a single target w_t (hollow circle) is pulled closer via the Tikhonov step while preserving other distances. (c) Cluster: a target set T (hollow red circles) is attracted with random sub-sampling per step, encouraging smooth blending across the cluster region.

5 Validation and Experimental Analysis

We validate MUSIC across three datasets of increasing complexity. *Gaussian mixtures* (Section 5.2) provide a controlled environment in which ground-truth geometry is known, allowing us to verify inversion accuracy, stability, and local correctness of the Jacobian model. *MNIST* (Section 5.3) tests whether the geometric machinery produces semantically meaningful interpolations on a real discrete manifold. *Labeled Faces in the Wild* (Section 5.4) probes robustness on high-dimensional, entangled visual data.

5.1 Continuity and Topology-Aware Metrics

To characterize the dynamical behavior of MUSIC trajectories across different datasets, we employ a set of continuity and topology-aware metrics. These quantities capture complementary aspects of the motion induced by the control updates, ranging from fine-grained local smoothness to large-scale geometric coherence. Because Self-Organizing Maps (SOMs) define a piecewise-linear partition of the input space, with Voronoi regions governed by individual prototypes, trajectory analysis must account for both continuous evolution within a region and discrete reorientations at region boundaries. The following metrics provide a comprehensive description of these phenomena and will be used throughout all experimental setups.

Step-direction continuity. A first measure of local smoothness is the cosine similarity between consecutive update directions,

$$C_t = \frac{\langle \Delta z_t, \Delta z_{t+1} \rangle}{\|\Delta z_t\| \|\Delta z_{t+1}\|}, \quad \Delta z_t = z_{t+1} - z_t.$$

Values $C_t \simeq 1$ indicate nearly collinear updates, whereas smaller or negative values reveal local directional reorientations.

Topology-aware continuity. Because a SOM induces a piecewise-linear tiling of the input space [2, 26], longer trajectories may cross the boundaries between Voronoi regions associated with different prototypes. At each crossing, the Jacobian structure changes and the optimal update direction is reoriented. To separate smooth evolution within a region from abrupt changes caused by boundary crossings, we evaluate all continuity metrics in a *topology-aware* manner conditioned on the evolution of the best-matching unit (BMU).

Transition rate. The *transition rate* quantifies how frequently the BMU changes along the path:

$$r_{\text{trans}} = \frac{1}{T} \sum_{t=0}^{T-1} \mathbf{1}[\text{BMU}(z_{t+1}) \neq \text{BMU}(z_t)].$$

Low values correspond to motion within a single basin of attraction; higher values reflect lattice traversal and frequent region crossings.

Dwell statistics. Between two transitions, the trajectory remains associated with the same prototype. The number of consecutive steps spent within a region defines a *dwell length* L_k . The median and interquartile range (IQR) of the set $\{L_k\}$ quantify the stability of residence within topological cells: longer dwell times correspond to stable local exploration, while short dwell times indicate rapid hopping between prototypes.

Curvature. The angular deviation between successive directions, $\theta_t = \cos^{-1}(C_t)$, provides a notion of local curvature. We normalize this by the step length to obtain the curvature per unit step,

$$\kappa_t = \frac{\theta_t}{\|\Delta z_t\|}.$$

We report median curvature separately for within-cell motion (κ_{within}) and across-cell transitions (κ_{trans}). Large κ_{trans} indicates the sharp reorientations produced at Voronoi boundaries.

Geodesic efficiency. To assess global coherence, we compare the total path length with the direct displacement between start and end points:

$$E_g = \frac{\|z_T - z_0\|}{\sum_{t=0}^{T-1} \|\Delta z_t\|}.$$

A value $E_g = 1$ corresponds to a perfectly straight trajectory, while smaller values indicate folded or meandering paths. Geodesic efficiency thus complements local metrics by quantifying long-range smoothness.

Segmented continuity. Finally, for each dwell segment (i.e., the interval between two BMU transitions), we compute the average step-direction continuity \bar{C}_k . The distribution of $\{\bar{C}_k\}$ captures the internal coherence of motion within stable regions. We report its median and interquartile range to characterize the variability of local behavior along the trajectory.

All continuity-based metrics (step continuity, curvature, geodesic efficiency, and segmented continuity) are unitless and invariant under uniform rescaling of the step sizes.

5.2 Synthetic validation on Gaussian mixture models

We first assess the proposed inversion and interpolation mechanisms in a controlled setting where both the data distribution and the prototype geometry are explicitly known. We consider a three-component Gaussian Mixture Model (GMM) in \mathbb{R}^D (here $D = 10$), whose component means forming a triangle in the first two coordinates, while the remaining dimensions contain small isotropic noise. From 25,000 samples we train a rectangular 20×20 SOM; an independent test set of 8,000 points is standardized using the same statistics. All experiments in this subsection operate directly in the standardized space.

Given a test point z and its best-matching prototype r , the inversion procedure constructs the anchored linear system $Bz = c$ from squared-distance activations (Section 2.1), where each row of B encodes an affine difference between prototype r and another prototype. Using a subset of N prototypes yields an $N \times D$ system. For each test point and for $N \in \{1, \dots, N_{\text{max}}\}$, we form the least-squares estimate $\hat{z} = B^+c$ and record the reconstruction error $\|z - \hat{z}\|_2$. Theory predicts that inversion is unstable when $N < D$ (under-determined system) and becomes exact as soon as B attains full column rank, i.e., once the selected prototypes span a D -dimensional affine subspace.

Figure 5 shows the median error across 1,500 test points as N increases. The error remains large and slowly decreasing for $N < D$, then drops abruptly to numerical zero at $N = D$ and stays there for all $N > D$. This provides a direct empirical confirmation that the distance-based linear system is essentially lossless once a full-rank set of prototypes is used. This outcome is expected: since squared-distance activations are quadratic in z , the anchored system of activation differences is exactly linear, and the Jacobian model introduces no approximation error (Section 3).

Beyond static inversion, the same GMM setting also allows us to study the *dynamics* induced by MUSIC in a structured, multi-modal manifold. On this triangular mixture, the trained SOM organizes its prototypes into three regions aligned with the mixture components. We then examine two complementary trajectory regimes:

(a) Informed convergence toward a single prototype. In the first regime, all trajectories are attracted toward a fixed SOM prototype chosen near the mean of one GMM component. Initial states are sampled from all three clusters, so

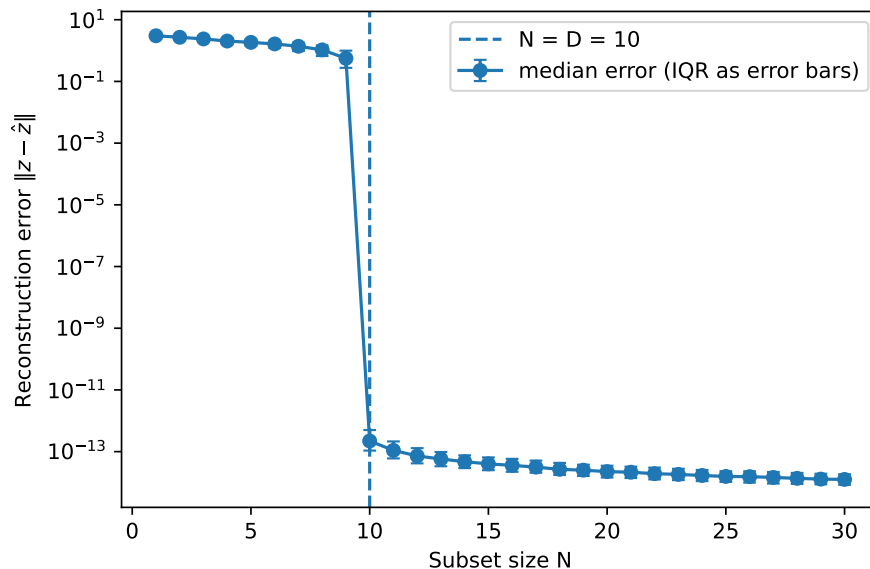


Figure 5: **Inversion accuracy on a Gaussian mixture.** Median reconstruction error $\|z - \hat{z}\|_2$ as a function of the subset size N used to build the anchored system $Bz = c$ from squared-distance activations. A 20×20 SOM is trained on a $D = 10$ GMM; errors are averaged over 1,500 test points, with error bars denoting the interquartile range. The dashed vertical line marks the intrinsic dimension D . In line with the theoretical analysis, inversion is unstable for $N < D$ but collapses to machine precision at $N = D$, and remains at the numerical floor for all overdetermined systems $N > D$, confirming that squared activations carry enough geometric information to recover the input uniquely.

starting points are topologically diverse. The MUSIC update rule generates sequences that move toward the selected prototype (with optional small Gaussian noise). Despite crossing multiple Voronoi boundaries, trajectories remain locally smooth with low within-cell curvature and converge to the same attractor, illustrating a globally coherent flow field capable of targeting isolated semantic anchors.

(b) Local exploration of a cluster-specific neighbourhood. In the second regime, the target at each step is chosen at random among the prototypes belonging to a selected cluster. Trajectories again start from all three mixture components: they are first pulled into the corresponding prototype region and then wandered within it, showing short dwell lengths, frequent BMU transitions, and moderate curvature. This behavior reflects a multi-scale organization: MUSIC guides points into the appropriate semantic basin at a global scale, while locally it induces piecewise-linear exploration constrained by the SOM topology.

To complement the qualitative trajectory plots, we report in Table 1 a set of global scalar metrics that summarize the behaviour of MUSIC dynamics on the GMM manifold. We focus on the topology-aware measures defined in Section 5.1: transition rate, dwell statistics, step-direction continuity, curvature, geodesic efficiency, and segmented continuity.

The metrics reveal a clear contrast between the two dynamical regimes. In the informed-convergence setting, the transition rate is low and dwell times are long, reflecting coherent motion within stable Voronoi regions. Step-direction continuity remains high and geodesic efficiency is close to 1, indicating globally directed flow toward the designated prototype. In the cluster-exploration regime, transitions are frequent and dwell times shrink to one or two steps. Continuity decreases, curvature becomes more variable, and geodesic efficiency drops substantially, consistent with locally wandering, topology-constrained motion within the selected mixture component. Together, these experiments show how MUSIC behaves on a simple multimodal manifold: through *directed* convergence to a single prototype and *exploratory* motion confined to a cluster-specific region.

5.3 Experiments on MNIST

We train a 32×32 toroidal SOM on the MNIST handwritten digit dataset [27] after full-dimensional PCA whitening. The toroidal topology avoids boundary artefacts and forces all classes to be embedded in a common continuous latent surface. By assigning each prototype the majority label of its BMU matches, we obtain ten coherent prototype

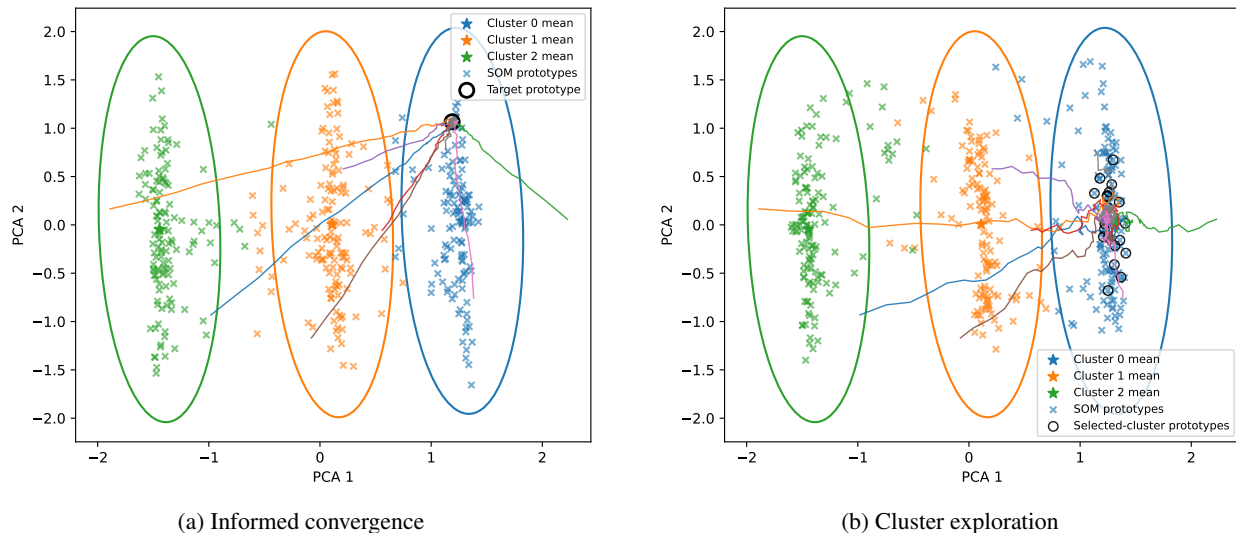


Figure 6: **Trajectory behavior on a three-cluster GMM manifold.** A SOM is trained on a triangular GMM, yielding three prototype regions (colours indicate assignment to the nearest mixture component). **(a)** MUSIC trajectories initialized from all clusters converge toward a single target prototype (circled), following smooth paths with low curvature even across Voronoi boundaries. **(b)** When the target at each step is sampled randomly from the prototypes of one cluster, trajectories are first attracted into that mode and then follow short, piecewise-linear exploratory segments within it. Ellipses show the 2σ covariance contours of the three GMM components.

Metric	Median \pm IQR
Transition rate r_{trans}	0.042 ± 0.021
Dwell length (steps)	6.0 ± 10.25
Dwell IQR	17.38 ± 12.50
Step-direction continuity C	0.291 ± 0.093
Curvature κ	34.86 ± 7.12
Geodesic efficiency E_g	0.757 ± 0.089
Segmented continuity \bar{C}_k	0.944 ± 0.362
Segmented continuity IQR	0.364 ± 0.188

(a) Informed convergence

Metric	Median \pm IQR
Transition rate r_{trans}	0.383 ± 0.100
Dwell length (steps)	1.5 ± 1.13
Dwell IQR	1.75 ± 1.44
Step-direction continuity C	0.079 ± 0.274
Curvature κ	9.42 ± 0.93
Geodesic efficiency E_g	0.291 ± 0.059
Segmented continuity \bar{C}_k	-0.007 ± 0.328
Segmented continuity IQR	0.475 ± 0.165

(b) Cluster exploration

Table 1: **Quantitative analysis of MUSIC trajectories on the GMM manifold.** Each entry reports the median \pm IQR across trajectories. **(Left)** Informed convergence: trajectories exhibit low transition rate, long dwell times, higher global step-direction continuity, and high geodesic efficiency, indicating globally directed motion toward a single prototype. **(Right)** Cluster exploration: trajectories undergo frequent BMU transitions, short dwell times, lower continuity, and reduced geodesic efficiency, reflecting locally wandering, topology-constrained exploration within the selected mixture component.

regions corresponding to the ten digit classes (Fig. 7). Neighbouring prototypes within each region represent smooth morphological variations (stroke thickness, orientation, style), while transitions between classes occur along contiguous boundaries where prototype basins meet. This topological structure provides the latent geometry on which MUSIC trajectories operate.

5.3.1 Inversion behaviour on MNIST

Before analysing MUSIC trajectories, we verify that the inversion mechanism derived in Section 2.1 remains numerically stable on real data. For each MNIST test image, we compute squared-distance activations from the SOM prototypes, form the anchored system $Bz = c$, and recover $\hat{z} = B^+c$. Because the map contains many more than D prototypes spanning the whitened PCA space in general position, the systems are highly overdetermined, and reconstruction errors $\|z - \hat{z}\|_2$ are consistently near machine precision. This guarantees that intermediate MUSIC states can be faithfully decoded back into pixel space.

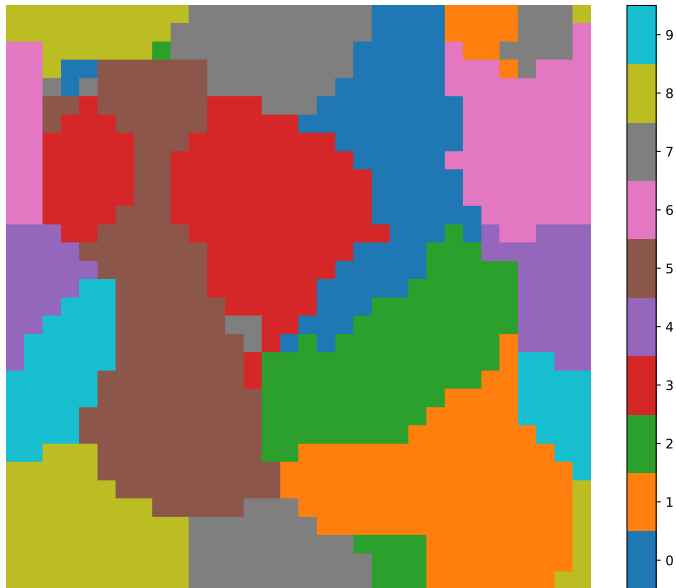


Figure 7: **Prototype organization on MNIST.** A 32×32 toroidal SOM trained on PCA-whitened MNIST forms ten coherent prototype regions corresponding to the digit classes. Neighbouring prototypes capture smooth morphological variations, while class boundaries emerge along contiguous regions of the map.

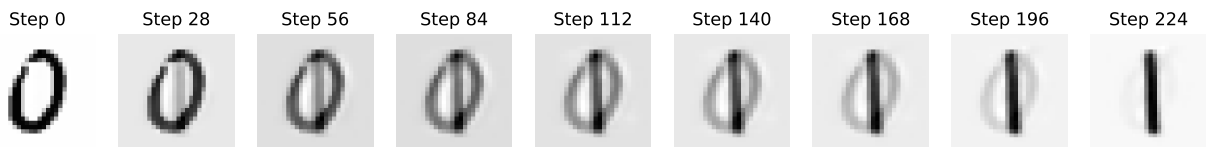


Figure 8: **MUSIC trajectory from “0” to “1” on MNIST (Tikhonov variant).** Starting from a test image of the digit “0” (left), MUSIC is run in informed mode toward a target prototype representing the digit “1” (right) using the Tikhonov-regularized update rule. The intermediate reconstructions exhibit a smooth and interpretable evolution: the circular stroke of the “0” gradually fades while a vertical segment progressively appears and sharpens. Around the middle of the path, both structures are partially visible, forming a hybrid configuration that reflects the proximity of the two class regions on the SOM. These intermediate states result from manifold-aware latent updates rather than pixel-space interpolation, and the Tikhonov formulation yields a particularly stable, smooth transition.

5.3.2 Directed class transition

We analyse a cross-class MUSIC interpolation from a digit “0” toward a prototype representing “1” (Fig. 8). Initially, the updates deform the “0” while preserving its circular outline. As the trajectory approaches the boundary between the “0” and “1” prototype regions, a hybrid configuration emerges: the loop becomes fainter while a vertical stroke begins to appear. After crossing the boundary, the trajectory aligns with the “1” region and converges smoothly toward the target prototype.

To quantify the smoothness of the latent trajectory beyond visual inspection (Fig. 9), we compute cosine similarities between successive update directions, $\cos(\Delta z_t, \Delta z_{t+1})$, and between each update and the initial direction, $\cos(\Delta z_t, \Delta z_0)$. The first remains consistently close to 1 throughout, indicating that consecutive steps are almost perfectly aligned. The second decreases steadily, revealing a gradual reorientation as the path crosses several Voronoi boundaries. This illustrates the expected two-scale structure of MUSIC: locally coherent, low-curvature motion within Voronoi regions, together with a global bending as the trajectory moves from the “0” region toward the “1” prototype.

5.3.3 Classifier confidence along trajectories

To assess whether intermediate MUSIC states remain semantically valid, we train an MLP classifier in the SOM’s PCA-whitened latent space (validation accuracy 98.0%) and evaluate the predicted class probabilities at every step

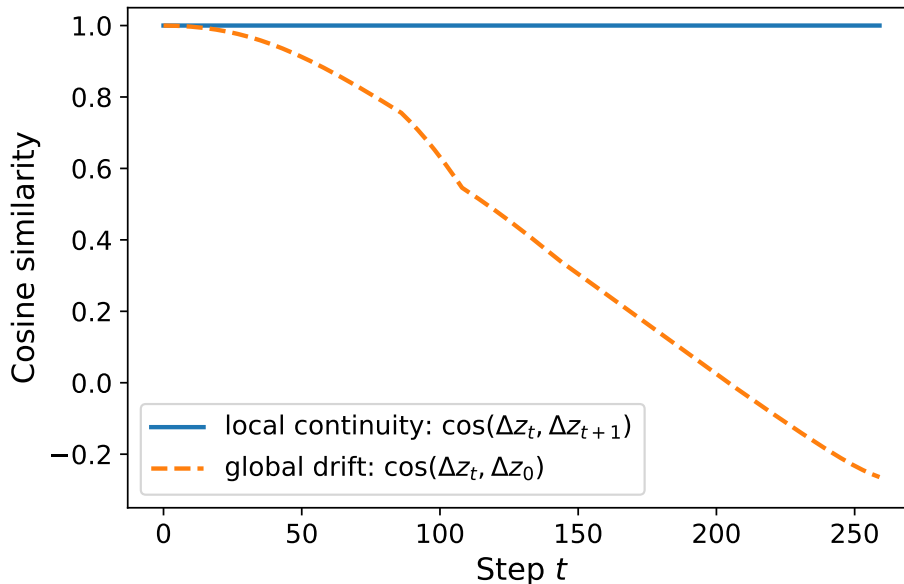


Figure 9: **Step-direction continuity on the MNIST “0”→“1” transition.** We report the cosine similarity between successive update directions, $\cos(\Delta z_t, \Delta z_{t+1})$, and between each update and the first one, $\cos(\Delta z_t, \Delta z_0)$, along the informed trajectory. The high local similarity (solid line) shows that consecutive steps remain nearly collinear, confirming the smoothness of MUSIC updates in the latent space. The gradual decay of global similarity (dashed line) reflects the expected reorientation of the trajectory as it crosses multiple Voronoi regions on the SOM while moving from the “0” manifold toward the “1” prototype. Together, these curves quantify the locally coherent yet globally bending nature of the MUSIC flow on a real data manifold.

along the $0 \rightarrow 1$ trajectory of Fig. 8. We compare MUSIC with a linear interpolation baseline that moves along the straight line from the source image to the target prototype in the same latent space.

Figure 10 shows the resulting confidence profiles. Both methods maintain high mean confidence (0.974 for MUSIC, 0.973 for linear), but differ sharply in their transition dynamics. MUSIC crosses from the source to the target class at step 87 (34.8% of the trajectory), whereas linear interpolation crosses only at step 139 (55.6%). More revealing is the sequence of predicted labels. MUSIC follows a clean $0 \rightarrow 0 \rightarrow 1 \rightarrow 1$ progression, passing through the “8” class for a single boundary step before committing to the target. Linear interpolation, by contrast, enters the “8” region at step 131 and remains there for 24 consecutive steps before finally reaching “1” at step 155. This prolonged detour through a semantically unrelated class reflects the straight-line path cutting across the SOM lattice without regard for prototype topology, while MUSIC follows the Voronoi structure and transitions directly between neighbouring class basins.

5.3.4 Comparison with VAE interpolation

We compare MUSIC trajectories with latent-space interpolation in a Variational Autoencoder (VAE) trained on the same MNIST data (32-dimensional latent space, 30 epochs). For each trajectory from the “0” source to the “1” target, we measure two complementary metrics: the mean k -nearest-neighbour distance to the training set (manifold proximity) and the mean Laplacian sharpness of the reconstructed images.

The VAE stays marginally closer to the data manifold (mean distance 3.93 vs. 4.08 for MUSIC and 4.10 for linear interpolation), owing to its learned decoder prior which pulls outputs toward the training distribution. However, MUSIC produces the sharpest intermediate images (sharpness 0.051 vs. 0.038 for VAE and 0.047 for linear), reflecting the fact that MUSIC reconstructions are anchored to specific prototypes rather than smoothed by a decoder bottleneck. This tradeoff—slightly farther from the data centroid but structurally sharper—is consistent with MUSIC operating on the discrete SOM geometry rather than on a smooth probabilistic manifold.

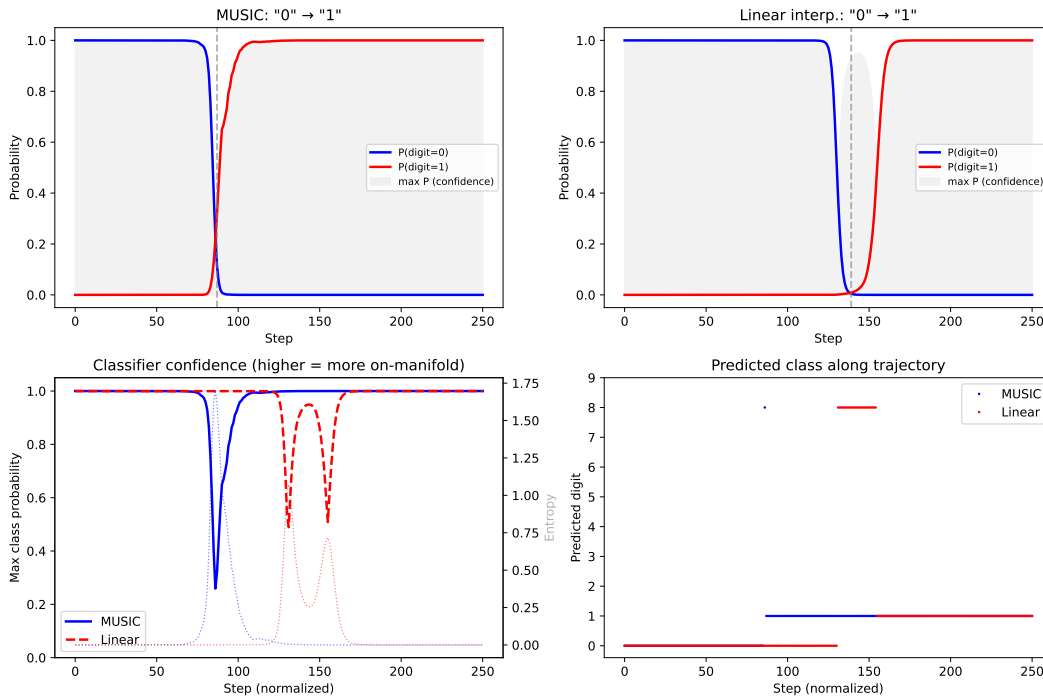


Figure 10: **Classifier confidence along the 0→1 trajectory.** An MLP classifier (validation accuracy 98.0%) evaluates the predicted class probabilities at each step. MUSIC (left) transitions from “0” to “1” at step 87 via a single boundary step through “8”, while linear interpolation (right) lingers in the “8” region for 24 consecutive steps before reaching “1” at step 155.

Table 2: **Systematic comparison of MUSIC vs. linear interpolation on MNIST** (10 digit pairs \times 3 samples = 30 trajectories per method). Each cell reports median \pm IQR. Bold indicates the statistically better method (Wilcoxon signed-rank test, $p < 0.05$); “ns” denotes no significant difference.

Metric	MUSIC	Linear	Sig.
Mean confidence	0.978 \pm 0.053	0.987 \pm 0.012	ns ($p=0.70$)
Min confidence	0.728 \pm 0.224	0.615 \pm 0.209	8/10 pairs
Mean sharpness	0.146 \pm 0.035	0.117 \pm 0.020	$p=0.002$
Manifold distance	7.11 \pm 0.86	5.94 \pm 0.52	$p=0.002$
Geodesic efficiency	0.738 \pm 0.094	1.000 \pm 0.000	—
Step continuity	0.942 \pm 0.116	1.000 \pm 0.000	—

5.3.5 Systematic evaluation across digit pairs

To confirm that the preceding observations generalise beyond a single pair, we evaluate MUSIC and linear interpolation across ten diverse digit pairs ($0 \rightarrow 1$, $1 \rightarrow 7$, $2 \rightarrow 3$, $3 \rightarrow 8$, $4 \rightarrow 9$, $5 \rightarrow 6$, $6 \rightarrow 0$, $7 \rightarrow 2$, $8 \rightarrow 5$, $9 \rightarrow 4$), with three independent starting images per pair, yielding 60 trajectories in total. Table 2 summarises the results.

Mean classifier confidence is comparable between the two methods ($p=0.70$), confirming that MUSIC trajectories stay within recognisable digit regions to the same degree as straight-line paths. MUSIC achieves significantly higher minimum confidence, winning on 8 out of 10 pairs: the worst-case intermediate frame is more recognisable with MUSIC than with linear interpolation. Image sharpness favours MUSIC on all 10 pairs ($p=0.002$), consistent with the prototype-anchored nature of the updates.

The tradeoff is path length: MUSIC’s geodesic efficiency averages 0.74, reflecting the piecewise-linear routing through Voronoi regions. Linear interpolation achieves $E_g=1$ by definition, but at the cost of the semantic detours documented above. Mean manifold distance is accordingly higher for MUSIC (7.11 vs. 5.94, $p=0.002$), because the curved path visits a broader portion of the latent space rather than cutting through low-density regions.



Figure 11: **Free evolution in latent space under geometry-aware control.** Starting from the same input face (left), we repeatedly apply random perturbations to the squared distance of a randomly selected SOM prototype. In the *MUSIC* row (top), each perturbation is processed through manifold-aware inversion: the update direction is chosen to satisfy the perturbed distance while preserving a small subset of nearby prototype distances, and the resulting step is normalized to a fixed magnitude. In the *no-constraints* row (bottom), the latent update is taken along the purely radial direction of the selected prototype, with the same step length but without any geometric preservation. Despite identical latent step sizes, the unconstrained trajectory rapidly drifts off the face manifold and produces distorted images, whereas MUSIC yields smooth, semantically coherent transformations that preserve the overall facial structure.

5.3.6 Hyperparameter sensitivity

We sweep the main MUSIC parameters on the $0 \rightarrow 1$ trajectory (150 steps) to characterise the stability of the method.

Preservation weight γ . Varying γ over $[0.5, 0.99]$ while holding $\lambda = 2 \times 10^{-4}$ and $\eta = 0.08$, mean classifier confidence remains between 0.950 and 0.958, confirming that the method is robust to this parameter. Step-direction continuity decreases moderately from 0.70 to 0.64 and geodesic efficiency increases from 0.60 to 0.75 as γ grows, reflecting the expected shift from exploration toward target-directed motion.

Tikhonov parameter λ . The regularisation strength λ exhibits textbook behaviour. At very low regularisation ($\lambda = 10^{-6}$), confidence reaches 0.9999 but continuity drops to -0.12 , indicating erratic, high-frequency steps that remain on-manifold but lack directional coherence. As λ increases from 10^{-5} to 10^{-3} , continuity rises from 0.43 to 0.67 while confidence stabilises around 0.95, yielding the recommended operating range. At $\lambda = 10^{-1}$, continuity reaches 0.999 and the flow becomes ultra-smooth but nearly stationary (convergence ratio 0.03). This validates the L-curve heuristic suggested in Section 4.

Target gain η . In the informed (single-target) mode, η has no measurable effect: all metrics remain identical across $[0.01, 0.20]$. This is expected from the theory: with a single target row in B_T , η scales only the magnitude of Δz , which is subsequently clipped by the step-size parameter ρ . The direction of the update is therefore invariant to η ; this parameter becomes relevant only in cluster mode, where it balances the contributions of multiple target prototypes.

5.4 Experiments on Faces in the Wild

We use a “Faces in the Wild” dataset [28], encode each image into a 512-dimensional latent vector via a pretrained autoencoder, and apply PCA whitening. A 32×32 SOM trained on these latent codes organizes faces according to broad semantic attributes—gender, skin tone, hairstyle, facial structure, and illumination—yielding a rich topological landscape suitable for controlled semantic explorations.

Free evolution. To illustrate the semantic benefits of geometry-aware inversion, we perform a free-evolution experiment starting from the same reference face. At each step, we randomly select a SOM prototype and impose a random perturbation of its squared distance. In the *MUSIC* condition, the update direction is obtained via our manifold-consistent inversion (preserving a small set of distances while driving the selected one), and the latent step is normalized to a fixed magnitude. In the *no-constraints* baseline, the latent update is instead taken along the purely radial direction of that prototype, without any geometric preservation.

Although both trajectories have identical step lengths in latent space, their qualitative behaviour differs drastically. The unconstrained trajectory rapidly drifts into implausible regions, yielding distorted faces. In contrast, the MUSIC

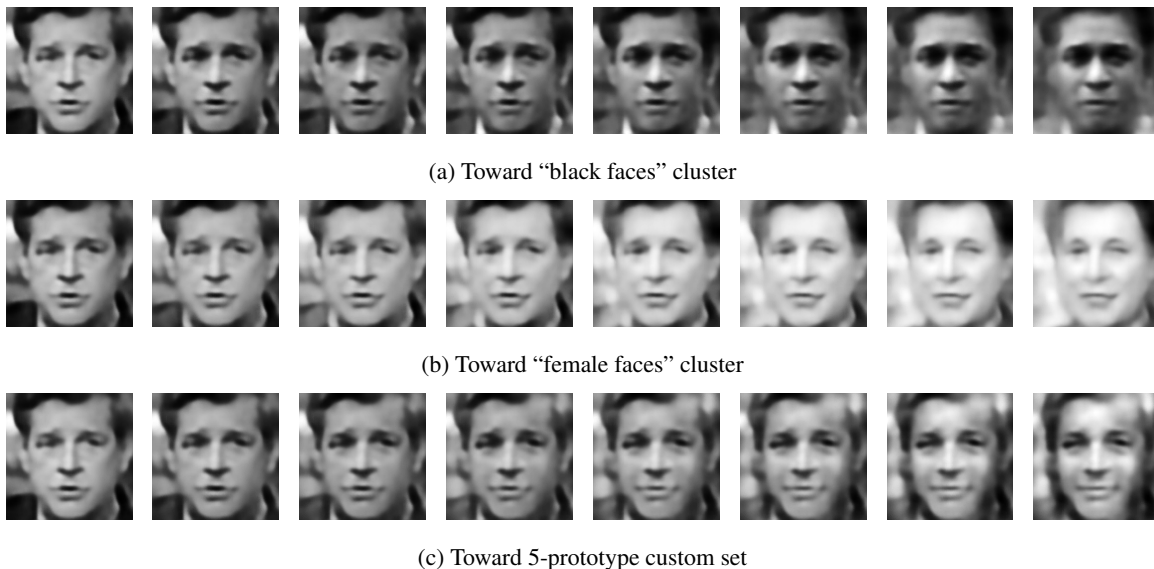


Figure 12: **MUSIC informed explorations on the facial manifold.** Starting from the same validation image (leftmost column), MUSIC moves along smooth, semantically meaningful directions induced by SOM topology. Each trajectory is guided by repeatedly selecting a single prototype from the target set. The input face is taken from the held-out validation set and was not used during SOM training.

trajectory evolves smoothly and remains on the face manifold, exhibiting coherent semantic transformations without collapsing into artifacts (Fig. 11). For a more detailed description of this experiment, refer to Supplementary Section S7.

Informed exploration toward semantic clusters. Beyond local transformations, MUSIC exhibits structured global behavior: when iterated with consistent prototype selections, the latent trajectory converges toward the corresponding cluster. We run MUSIC in informed mode, where at each step the update is directed toward a single prototype selected from a user-chosen target cluster. This one-prototype-at-a-time guidance produces smooth, decoder-faithful trajectories that remain close to the learned manifold. A key property is identity preservation: because each step is constrained by the local SOM geometry, core identity cues remain stable until the trajectory approaches the target region, while attributes such as skin tone or facial softness evolve gradually.

We illustrate three explorations, each probing a distinct semantic direction on the SOM (Fig. 12):

(a) Transition toward a demographic region. Starting from a validation image, we guide the trajectory toward a cluster containing predominantly darker-skinned faces. The evolution shows a smooth darkening of skin tone and gradual adjustments in local shading and facial texture, while identity remains stable deep into the trajectory.

(b) Transition toward a gender-specific region. Using the same initial face, we target a cluster of mainly female prototypes. The resulting path progressively introduces features associated with the cluster—subtle changes in eyes, eyebrows, and facial softness—without abrupt distortions.

(c) Convergence toward a small user-defined prototype set. To test MUSIC in a minimally constrained setting, we select five prototypes at random (not forming a labelled cluster) and use them as informed anchors. The trajectory remains stable and interpretable, moving toward a mixed semantic region combining attributes of the selected prototypes.

To quantitatively verify that informed trajectories reach their intended semantic regions, we measure—for the experiment targeting the “female” cluster—the mean Euclidean distance between the latent state z_t and all prototypes in that cluster. As shown in Fig. 13, the distance decreases smoothly and monotonically, confirming that the latent dynamics consistently move toward the target region.

Comparison with linear interpolation. For a single face-to-prototype transition, linear interpolation in the 512-dimensional latent space produces very similar results, indicating that the autoencoder space is already locally Euclidean

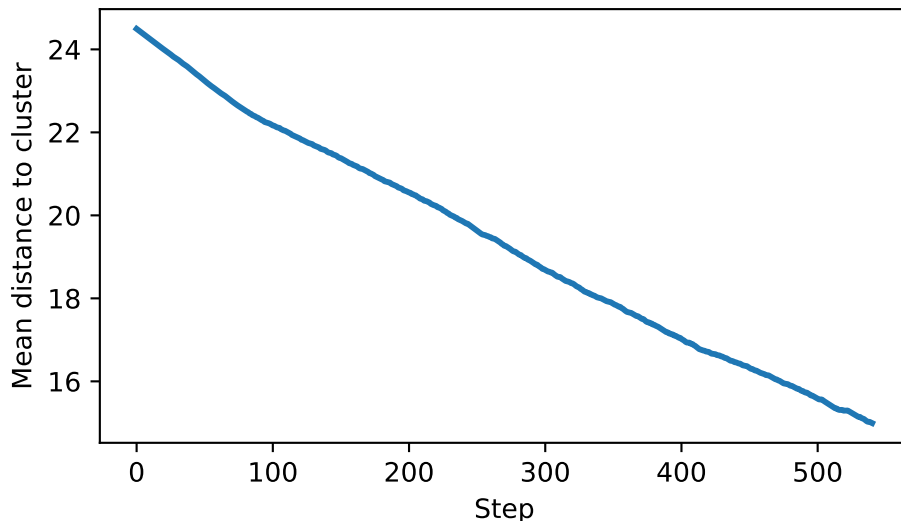


Figure 13: **Convergence toward the target prototype cluster.** Mean Euclidean distance between z_t and the “female” cluster prototypes along the trajectory of Fig. 12(b). The monotonic decay confirms directed motion toward the target region.



Figure 14: **MUSIC vs. linear interpolation toward a target facial cluster.** MUSIC (top row) preserves identity and produces sharp intermediate faces, while linear interpolation (bottom row) collapses toward a blurred cluster mean. Both trajectories target the female-faces cluster.

along this direction. We therefore consider a stronger baseline: linear interpolation from the initial face to the *mean* of the target cluster (the same female-faces cluster used above).

This comparison isolates two different mechanisms. Linear interpolation moves straight toward the cluster barycenter, effectively averaging all facial features and producing increasingly blurred, identity-agnostic faces. Informed MUSIC instead follows a piecewise-smooth trajectory guided by actual prototypes; every intermediate point remains close to a real face embedding, preserving structure and identity.

Figure 14 illustrates these effects: the linear path collapses rapidly into a blurry representation, while MUSIC produces sharper, more realistic intermediate faces with the original identity preserved deep into the sequence. The accompanying metric plots (Fig. 15) confirm this quantitatively. Linear interpolation reduces the cluster distance aggressively (from ~ 25 to ~ 3) but causes identity drift climbing to ~ 800 , whereas MUSIC converges more moderately (to ~ 15) while maintaining near-zero identity drift throughout.

For reproducibility, all experiments on faces were performed using a single fixed configuration of MUSIC hyperparameters ($\gamma = 0.85$, $\lambda = 10^{-4}$, $\rho = 0.1$, $\eta = 0.04$, $\sigma = 0.01$), ensuring that the observed behaviours arise from the method itself rather than from per-sample tuning.

Overall, these experiments demonstrate that MUSIC remains stable and semantically meaningful on a highly nonlinear manifold of real faces. Despite the complex entanglement of identity, pose, illumination, and demographic attributes,

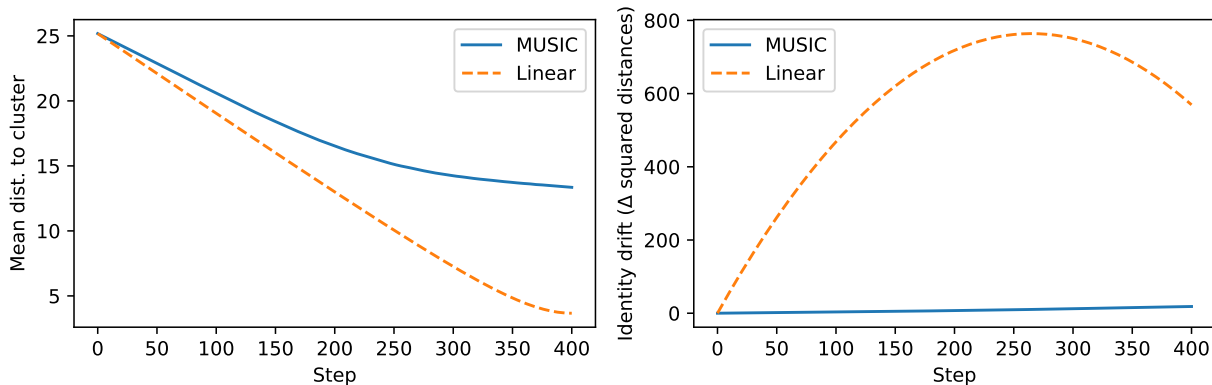


Figure 15: **Convergence and identity drift during MUSIC vs. linear transition.** (Left) Mean distance to the female-faces cluster. Linear interpolation collapses to the cluster barycenter, while MUSIC approaches the cluster more conservatively. (Right) Identity drift relative to initial anchors. MUSIC preserves identity for most of the trajectory, whereas linear interpolation causes a dramatic loss (up to ~ 800) before partially recovering near its endpoint.

informed MUSIC trajectories perform long-range semantic transitions while preserving photometric consistency and remaining within the domain of valid decoder embeddings.

6 Discussion

A central insight of this work is that the structure of the prototype set plays a crucial role in the stability and interpretability of the resulting trajectories. While the inversion mechanism requires only $N \geq D+1$ affinely independent vectors, the behaviour of MUSIC depends strongly on how these reference points are organized in space. If prototypes are sampled randomly or obtained from unstructured clustering, the resulting Voronoi cells have no coherent semantic geometry: neighbourhoods do not correspond to gradual attribute changes, boundary transitions occur abruptly, and intermediate states are difficult to interpret. In such settings, MUSIC produces unstable or chaotic motion because the underlying partition lacks topological meaning.

In contrast, a Self-Organizing Map provides a two-dimensional, topology-preserving lattice in which neighbouring prototypes correspond to semantically similar inputs. This induces smooth Voronoi regions and contiguous boundaries that together form a piecewise-linear coordinate chart of the data manifold. MUSIC leverages precisely this structure: within a single region, the Tikhonov-regularized flow produces low-curvature motion aligned with local prototype geometry, while boundary crossings occur in a predictable manner reflecting the lattice topology. The systematic evaluation on MNIST confirms this empirically: MUSIC achieves significantly higher image sharpness than linear interpolation on all ten digit pairs tested ($p=0.002$; Table 2), reflecting the prototype-anchored nature of the updates. This behaviour cannot be replicated by standard clustering methods such as k -means or k NN grouping, which lack neighbourhood continuity and provide no global topological backbone for guiding semantic transformations.

Viewed from this perspective, MUSIC offers a deterministic, geometry-driven mechanism for semantic interpolation that complements modern generative models. Whereas VAEs or diffusion models define trajectories through neural parameterisation or stochastic sampling, MUSIC defines them through prototype geometry and linear algebra alone. A direct comparison on MNIST illustrates the tradeoff: a VAE trained on the same data stays marginally closer to the data manifold (mean k -NN distance 3.93 vs. 4.08), but MUSIC produces the sharpest intermediate images (Laplacian sharpness 0.051 vs. 0.038; Section 5.3.4). This reflects a fundamental distinction: the VAE decoder smooths outputs toward the training distribution, while MUSIC reconstructions remain anchored to discrete prototypes and preserve structural detail. Both approaches thus provide interpretability—MUSIC through geometric transparency, generative models through probabilistic structure—and may be profitably combined.

A comparison with linear interpolation in the autoencoder latent space further clarifies the behaviour of MUSIC. The classifier confidence experiment (Section 5.3.3) reveals a striking qualitative difference on the $0 \rightarrow 1$ trajectory: MUSIC transitions directly between the two class basins, passing through the “8” boundary region for a single step, whereas linear interpolation lingers in the “8” class for 24 consecutive steps before reaching the target. This pattern generalises across digit pairs: in the systematic evaluation, MUSIC achieves higher minimum confidence on 8 out of 10 pairs (Table 2), indicating that its worst-case intermediate frames remain more recognisable. When moving toward an entire

semantic cluster on faces, the advantage becomes even more pronounced: straight-line interpolation collapses toward the barycentric mean, producing a blurred and unrealistic face, whereas MUSIC follows prototype transitions and maintains identity much longer (Fig. 15). The price is a longer path through the latent space (geodesic efficiency 0.74 vs. 1.0), which is the expected cost of following the SOM topology rather than cutting through low-density regions.

From a computational standpoint, each MUSIC update requires solving a D -dimensional linear system of the form

$$((1 - \gamma)A^\top A + \gamma B^\top B + \lambda I) \Delta z = r,$$

where A and B contain only a small number of Jacobian rows associated with preserved and target prototypes. Since these matrices are extremely low rank relative to D , the computational cost is dominated by operations linear in the latent dimension. This makes MUSIC substantially lighter than diffusion models or autoregressive architectures, which require a full neural forward pass at every iteration. Moreover, the method does not require a generative decoder unless visual inspection of intermediate states is desired.

The hyperparameter analysis (Section 5.3.6) confirms that the method is robust in practice. Mean classifier confidence varies by less than one percentage point across the full range of the preservation weight $\gamma \in [0.5, 0.99]$. The Tikhonov parameter λ exhibits textbook regularisation behaviour, with a well-defined operating regime between 10^{-5} and 10^{-3} where continuity and convergence are jointly favourable; this validates the L-curve heuristic suggested in Section 4. The target gain η is provably irrelevant in single-target mode (the step-size clipping absorbs the scaling), but becomes active in cluster mode where it balances multiple target contributions.

The method naturally inherits some limitations. Exact inversion is guaranteed only when the prototypes span the latent space, which may fail if the intrinsic dimension exceeds the number of prototypes or if prototypes are poorly distributed. In practice, this is mitigated by dimensionality reduction (e.g. PCA) or by using larger or adaptive prototype sets, such as Growing Neural Gas or Dynamic SOMs. Furthermore, since the SOM provides a piecewise-linear approximation to the data manifold, the resulting trajectories follow the geometry of the map rather than the true underlying curvature; nevertheless, the flows observed in complex domains such as face embeddings remain stable and interpretable.

Finally, the generality of the approach extends beyond classical SOMs. Because the method relies only on prototype geometry and squared-distance structure, any architecture producing a set of reference vectors with topological organisation—Growing SOMs, hierarchical maps, SOM-VAE, neural gas, and related models—can serve as the backbone for inversion and for MUSIC trajectories. This creates a flexible bridge between competitive learning and modern latent representations, opening avenues for semantic editing, prototype-guided data augmentation, and interactive exploration of learned manifolds.

7 Conclusion

This work revisits Self-Organizing Maps through the lens of distance geometry and shows that their activation patterns contain sufficient information to recover the original input exactly. By interpreting the squared distances to prototypes as a structured system of affine constraints, we derived a linear inversion mechanism that is fully deterministic, geometrically grounded, and requires no probabilistic modeling. Building on this principle, we introduced MUSIC, a manifold-aware update rule that generates smooth and interpretable semantic trajectories on the prototype lattice. MUSIC combines the selective manipulation of squared distances with Tikhonov regularization, producing stable flows within Voronoi regions and controlled reorientations across their boundaries.

Across experiments on synthetic mixtures, handwritten digits, and facial images, MUSIC reveals how SOM structure shapes latent dynamics. On a GMM, the method exhibits the expected behaviour of a piecewise-linear flow driven by prototype geometry. On MNIST, it produces meaningful cross-class transitions with clear intermediate states and quantifiable continuity. On Labelled Faces in the Wild, MUSIC enables attribute-specific transformations and user-defined semantic edits while preserving identity and photometric coherence.

The quantitative evaluation on MNIST provides concrete evidence for the advantages of topology-guided interpolation. Across ten digit pairs, MUSIC produces significantly sharper intermediate images than linear interpolation ($p=0.002$, all pairs favouring MUSIC) and maintains higher minimum classifier confidence on the majority of transitions. A classifier confidence analysis reveals that MUSIC transitions directly between source and target class basins, while linear interpolation detours through semantically unrelated regions. The hyperparameter study confirms practical robustness: mean confidence varies by less than one percentage point across the full range of the preservation weight, and the Tikhonov parameter exhibits well-behaved regularisation dynamics consistent with the theory.

A key strength of the framework is its architectural generality. Because inversion and MUSIC rely solely on prototype coordinates and squared-distance geometry, they extend naturally to the whole family of prototype-based models: classical SOMs, Growing Neural Gas, Dynamic and Hierarchical SOMs, adaptive-topology variants, and hybrid

approaches such as SOM-VAE. In all cases, the prototypes provide the coordinate chart while MUSIC supplies the continuous dynamics.

The method also comes with clear limitations. Reconstruction fidelity is bounded by the expressiveness of the latent basis (e.g., PCA, autoencoder embeddings), and cannot match the realism of modern generative decoders. The SOM approximates the data manifold only piecewise linearly, so curvature is captured discretely rather than continuously. Nonetheless, these constraints are precisely what endow the approach with interpretability: prototype geometry makes latent transitions transparent, stable, and semantically meaningful.

Overall, this work bridges classical competitive learning with modern latent-space analysis. SOM inversion transforms prototype maps into deterministic coordinate charts, and MUSIC provides a mechanism for navigating them in a controlled, manifold-aware fashion. This combination enables interpretable semantic exploration, latent editing, and data augmentation, and indicates a broader role for prototype-based representations within geometric and generative machine learning.

References

- [1] Teuvo Kohonen. Self-organized formation of topologically correct feature maps. *Biological cybernetics*, 43(1):59–69, 1982.
- [2] Teuvo Kohonen. The basic som. In *Self-organizing maps*, pages 105–176. Springer, 2001.
- [3] Gert Hauske. A self organizing map approach to image quality. *Biosystems*, 40(1-2):93–102, 1997.
- [4] Teuvo Kohonen. *Self-organization and associative memory*, volume 8. Springer Science & Business Media, 2012.
- [5] Janne Nikkilä, Petri Törönen, Samuel Kaski, Jarkko Venna, Eero Castrén, and Garry Wong. Analysis and visualization of gene expression data using self-organizing maps. *Neural networks*, 15(8-9):953–966, 2002.
- [6] Juha Vesanto. *Data exploration process based on the self-organizing map*. Helsinki University of Technology, 2002.
- [7] Bernd Fritzsche. A growing neural gas network learns topologies. *Advances in neural information processing systems*, 7, 1994.
- [8] Daminda Alahakoon, Saman K. Halgamuge, and Bala Srinivasan. Dynamic self-organizing maps with controlled growth for knowledge discovery. *IEEE Transactions on neural networks*, 11(3):601–614, 2000.
- [9] Michael Dittenbach, Dieter Merkl, and Andreas Rauber. The growing hierarchical self-organizing map. In *Proceedings of the IEEE-INNS-ENNS International Joint Conference on Neural Networks. IJCNN 2000. Neural Computing: New Challenges and Perspectives for the New Millennium*, volume 6, pages 15–19. IEEE, 2000.
- [10] Vincent Fortuin, Matthias Hüser, Francesco Locatello, Heiko Strathmann, and Gunnar Rätsch. Som-vae: Interpretable discrete representation learning on time series. *arXiv preprint arXiv:1806.02199*, 2018.
- [11] Diederik P Kingma and Max Welling. Auto-encoding variational bayes. *arXiv preprint arXiv:1312.6114*, 2013.
- [12] Aaron Van Den Oord, Oriol Vinyals, et al. Neural discrete representation learning. *Advances in neural information processing systems*, 30, 2017.
- [13] Jonathan Ho, Ajay Jain, and Pieter Abbeel. Denoising diffusion probabilistic models. *Advances in neural information processing systems*, 33:6840–6851, 2020.
- [14] Leonard M. Blumenthal. *Theory and Applications of Distance Geometry*. Oxford University Press, 1953.
- [15] John Clifford Gower. Properties of euclidean and non-euclidean distance matrices. *Linear algebra and its applications*, 67:81–97, 1985.
- [16] Leo Liberti, Carlile Lavor, Nelson Maculan, and Antonio Mucherino. Euclidean distance geometry and applications. *SIAM review*, 56(1):3–69, 2014.
- [17] Thomas H Meyer and Ahmed F Elaksher. Solving the multilateration problem without iteration. *Geomatics*, 1(3):324–334, 2021.
- [18] Leonard Asimow and Ben Roth. The rigidity of graphs. *Transactions of the American Mathematical Society*, 245:279–289, 1978.
- [19] Teuvo Kohonen. The self-organizing map. *Proceedings of the IEEE*, 78(9):1464–1480, 1990.
- [20] Marie Cottrell, Jean-Claude Fort, and Gilles Pagès. Theoretical aspects of the som algorithm. *Neurocomputing*, 21(1-3):119–138, 1998.
- [21] Juha Vesanto. Som-based data visualization methods. *Intelligent data analysis*, 3(2):111–126, 1999.
- [22] Kimmo Kiviluoto. Topology preservation in self-organizing maps. In *Proceedings of International Conference on Neural Networks (ICNN'96)*, volume 1, pages 294–299. IEEE, 1996.
- [23] Pierre-Antoine Absil, Robert Mahony, and Rodolphe Sepulchre. *Optimization algorithms on matrix manifolds*. Princeton University Press, 2008.
- [24] Shun-ichi Amari. *Information geometry and its applications*, volume 194. Springer, 2016.
- [25] Per Christian Hansen. *Rank-deficient and discrete ill-posed problems: numerical aspects of linear inversion*. SIAM, 1998.
- [26] Hujun Yin. The self-organizing maps: background, theories, extensions and applications. In *Computational intelligence: A compendium*, pages 715–762. Springer, 2008.
- [27] Yann LeCun, Léon Bottou, Yoshua Bengio, and Patrick Haffner. Gradient-based learning applied to document recognition. *Proceedings of the IEEE*, 86(11):2278–2324, 1998.
- [28] Gary B Huang, Marwan Mattar, Tamara Berg, and Eric Learned-Miller. Labeled faces in the wild: A database for studying face recognition in unconstrained environments. In *Workshop on faces in 'Real-Life' Images: detection, alignment, and recognition*, 2008.

Supplementary Material

S1 Additional properties of the SOM activation map

This section collects three results on the SOM squared-distance activation map $f(z) = a(z)$ that complement the inversion theory developed in Section 2 of the main text. They are included here for completeness; no later derivation depends on them directly.

S1.1 Equivariance under rigid motions

A useful property of the activation map is its invariance under rigid motions applied jointly to the input and the prototypes. For any translation $t \in \mathbb{R}^D$ and orthogonal transformation $R \in O(D)$,

$$a_j(Rz + t) = \|Rz + t - (Rw_j + t)\|^2 = \|z - w_j\|^2 = a_j(z).$$

Hence, the activations depend only on the *relative* configuration of z and $\{w_j\}$, not on the absolute position or orientation of the point cloud. This confirms that centering or whitening the prototypes (as recommended in Section 2) does not alter the activation pattern and therefore cannot affect the inversion result.

S1.2 Full rank of the activation Jacobian

The main text states that the Jacobian of the activation map has full rank everywhere (used in the perturbation analysis of Section 3). We provide the proof here.

Lemma 1 (Full rank of the activation Jacobian). *Let $J(z) \in \mathbb{R}^{N \times D}$ be the Jacobian with rows $J_j(z) = \nabla_z a_j(z)^\top = 2(z - w_j)^\top$. If the prototypes $\{w_j\}$ contain $D+1$ affinely independent points, then $\text{rank } J(z) = D$ for all $z \in \mathbb{R}^D$.*

Proof. Fix any anchor r . Since $\{w_j - w_r\}_{j \neq r}$ span \mathbb{R}^D by assumption, the vectors $\{z - w_j\}_{j \neq r} = \{(z - w_r) - (w_j - w_r)\}_{j \neq r}$ span the same subspace. Hence the rows of $J(z)$ span \mathbb{R}^D , giving $\text{rank } J(z) = D$. \square

S1.3 Weighted least-squares inversion under correlated noise

Corollary 1 in the main text assumes i.i.d. activation noise. When the noise has a known covariance structure Σ (i.e., $\varepsilon \sim \mathcal{N}(0, \Sigma)$), a tighter reconstruction is obtained via weighted least squares:

$$\hat{z} = \arg \min_z \|(Bz - c)\|_{\Sigma^{-1}}^2 = (B^\top \Sigma^{-1} B)^{-1} B^\top \Sigma^{-1} c,$$

with stability now governed by the smallest eigenvalue of $B^\top \Sigma^{-1} B$. This is relevant whenever downstream noise sources (e.g., quantization or sensor error) introduce heteroscedastic perturbations to the activation vector.

S2 Radial-tangential decomposition and global isodistance preservation

Consider a fixed input $z \in \mathbb{R}^D$ and a set of SOM prototypes $\{w_j\}_{j=1}^N$. The squared-distance activation of prototype j is

$$a_j(z) = \|z - w_j\|^2,$$

with first-order change under a small perturbation Δz given by

$$\Delta a_j \approx 2(z - w_j)^\top \Delta z.$$

Thus, preserving the distance to prototype j to first order amounts to enforcing

$$(z - w_j)^\top \Delta z = 0,$$

i.e., Δz lies in the orthogonal complement of the radial direction $z - w_j$.

Fix a reference prototype w_k and define $x = z - w_k$. We decompose any perturbation as

$$\Delta z = \Delta z_{\parallel} + \Delta z_{\perp}, \quad \Delta z_{\parallel} = \alpha x, \quad x^\top \Delta z_{\perp} = 0.$$

By construction, the parallel component Δz_{\parallel} controls the first-order change of the distance to w_k , while the orthogonal component Δz_{\perp} lies in the tangent subspace of the local isodistance manifold around z relative to w_k .

To see why Δz_\perp also preserves the distances to *all* prototypes to first order, note that

$$z - w_j = (z - w_k) + (w_k - w_j) = x + c_j,$$

where $c_j = w_k - w_j$ is a constant vector independent of Δz . Hence the family of radial directions $\{z - w_j\}_{j=1}^N$ lies in an affine translate of the one-dimensional subspace spanned by x :

$$z - w_j \in x + \text{span}\{c_j : j = 1, \dots, N\}.$$

As a consequence, all first-order distance changes can be written as

$$\Delta a_j \approx 2(z - w_j)^\top \Delta z = 2(x + c_j)^\top \Delta z = 2x^\top \Delta z + 2c_j^\top \Delta z.$$

If we choose Δz_\perp such that $x^\top \Delta z_\perp = 0$, then

$$\Delta a_j^{(\perp)} \approx 2(z - w_j)^\top \Delta z_\perp = 2x^\top \Delta z_\perp + 2c_j^\top \Delta z_\perp = 2c_j^\top \Delta z_\perp.$$

The vectors $c_j = w_k - w_j$ are fixed prototype offsets that do not depend on the current point z . Although their magnitudes may vary across prototypes, the corresponding contributions $c_j^\top \Delta z$ remain uniformly bounded. In contrast, the shared term

$$x = z - w_k$$

captures the large-scale geometry of z relative to the SOM prototypes, and the component $x^\top \Delta z$ typically dominates the first-order variation of all squared distances. Thus, a perturbation Δz decomposes into a dominant component along x , which controls the primary variation of $\|z - w_j\|^2$, and a residual component orthogonal to x , whose effect is mediated only through the bounded offsets c_j . Consequently, the contribution of Δz_\perp to the squared distances is much smaller—effectively a second-order effect—compared to the variation produced by the component of Δz parallel to x .

Figure 3 illustrates this decomposition in \mathbb{R}^2 : the radial direction $x = z - w_k$ controls distance changes to the reference prototype, while tangential directions orthogonal to x induce negligible first-order changes in the distances to all prototypes.

Typical dependence on the ambient dimension D . The preceding argument shows that tangential motion eliminates the shared contribution $x^\top \Delta z$ and leaves only the residual terms $c_j^\top \Delta z_\perp$. To make the dependence on D explicit, we analyze the typical magnitude of these residual dot products when Δz_\perp is chosen without preferential alignment inside the $(D - 1)$ -dimensional subspace orthogonal to x .

Let $\mathcal{T} := \{u \in \mathbb{R}^D : x^\top u = 0, \|u\| = 1\}$ be the unit sphere in the tangential subspace, and write $\Delta z_\perp = \eta u$ with $u \in \mathcal{T}$ and step length $\eta > 0$. Since $u \perp x$, only the component of c_j orthogonal to x contributes:

$$c_{j,\perp} := \left(I - \frac{xx^\top}{\|x\|^2}\right)c_j, \quad c_j^\top u = c_{j,\perp}^\top u.$$

Assume that u is uniformly distributed on \mathcal{T} (i.e., an isotropic direction in the tangential subspace). By rotational invariance in the $(D - 1)$ -dimensional subspace, for any fixed vector v with $v \perp x$ and $\|v\| = 1$, the random variable $v^\top u$ has the same distribution as the first coordinate of a uniform point on \mathbb{S}^{D-2} . In particular, it is mean-zero, with variance

$$\mathbb{E}[(v^\top u)^2] = \frac{1}{D-1}. \quad (8)$$

Therefore, for each prototype j ,

$$\mathbb{E}[(c_j^\top u)^2] = \mathbb{E}[(c_{j,\perp}^\top u)^2] = \frac{\|c_{j,\perp}\|^2}{D-1}, \quad \Rightarrow \quad |c_j^\top \Delta z_\perp| \text{ is typically of order } \eta \frac{\|c_{j,\perp}\|}{\sqrt{D-1}}. \quad (9)$$

Recalling $\Delta a_j^{(\perp)} \approx 2c_j^\top \Delta z_\perp$, this yields the typical scaling

$$|\Delta a_j^{(\perp)}| \approx 2|c_j^\top \Delta z_\perp| \sim 2\eta \frac{\|c_{j,\perp}\|}{\sqrt{D-1}},$$

showing that tangential perturbations become increasingly close to isometries as D grows (in a typical-case sense).

A high-probability bound follows from standard concentration on the sphere. For u uniform on \mathcal{T} and any fixed $v \perp x$ with $\|v\| = 1$,

$$\mathbb{P}(|v^\top u| \geq t) \leq 2 \exp\left(-\frac{(D-2)t^2}{2}\right). \quad (10)$$

Applying (10) to $v = c_{j,\perp}/\|c_{j,\perp}\|$ and a union bound over $j = 1, \dots, N$ gives that, with probability at least $1 - \delta$,

$$\max_{1 \leq j \leq N} |c_j^\top u| = \max_{1 \leq j \leq N} |c_{j,\perp}^\top u| \leq \|c_\perp\|_{\max} \sqrt{\frac{2 \log(2N/\delta)}{D-2}}, \quad \|c_\perp\|_{\max} := \max_j \|c_{j,\perp}\|. \quad (11)$$

Hence,

$$\max_{1 \leq j \leq N} |\Delta a_j^{(\perp)}| \approx 2\eta \max_j |c_j^\top u| \lesssim 2\eta \|c_\perp\|_{\max} \sqrt{\frac{2 \log(2N/\delta)}{D-2}}. \quad (12)$$

This bound makes explicit that, as long as $D \gg \log N$, tangential steps are simultaneously near-isometric for all prototypes with high probability.

We stress that these scalings describe typical isotropic directions in the tangential subspace; they can be weakened if the latent geometry is strongly anisotropic or if the offsets $\{c_j\}$ are systematically aligned with a low-dimensional set of semantic directions.

S3 Tikhonov-regularized quadratic energy

The Manifold-Aware Unified SOM Inversion and Control (MUSIC) framework defines at each iteration a perturbation $\Delta z \in \mathbb{R}^D$ of an input vector z that modulates the squared distances to the prototypes $\{w_j\}_{j=1}^N$ of a Self-Organizing Map (SOM).

The activation of prototype j is $a_j(z) = \|z - w_j\|^2$ with Jacobian $J_j(z) = \nabla_z a_j(z) = 2(z - w_j)^\top$. For small displacements Δz , the first-order expansion $a_j(z + \Delta z) \approx a_j(z) + J_j(z)\Delta z$ describes the local change in activation space.

Given a subset S of prototypes whose activations should remain approximately constant (preservation set) and a subset T whose activations should change toward prescribed values (target set), one defines row-normalized Jacobians $A_S \in \mathbb{R}^{|S| \times D}$ and $B_T \in \mathbb{R}^{|T| \times D}$, together with a target activation increment $b \in \mathbb{R}^{|T|}$.

The preservation constraint is $A_S \Delta z \approx 0$, while the attraction constraint is $B_T \Delta z \approx b$. Because these constraints may be redundant or inconsistent, MUSIC formulates the update as the minimizer of a Tikhonov-regularized quadratic energy

$$E_\gamma(\Delta z) = (1 - \gamma)\|A_S \Delta z\|^2 + \gamma\|B_T \Delta z - b\|^2 + \lambda\|\Delta z\|^2, \quad \gamma \in [0, 1], \lambda > 0.$$

The first two terms correspond to preservation and attraction, balanced by the parameter γ , while the last term introduces a Tikhonov regularizer that stabilizes the inverse problem and controls the magnitude of the perturbation. The presence of $\lambda > 0$ ensures that the energy is strongly convex even when the Jacobians are rank-deficient, thus guaranteeing a unique and stable solution.

Let $H = (1 - \gamma)A_S^\top A_S + \gamma B_T^\top B_T + \lambda I_D$ and $r = \gamma B_T^\top b$. The minimizer Δz^* satisfies $\nabla E_\gamma(\Delta z) = 2(H\Delta z - r) = 0$ and is therefore

$$\Delta z^* = H^{-1}r = \left((1 - \gamma)A_S^\top A_S + \gamma B_T^\top B_T + \lambda I \right)^{-1} \gamma B_T^\top b.$$

Since $H - \lambda I$ is positive semidefinite, and λI is positive definite ($H \succeq \lambda I \succ 0$), the solution exists, is unique, and depends smoothly on the data.

S4 Tikhonov regularization

The term ‘‘Tikhonov regularization’’ refers to the fact that $\lambda\|\Delta z\|^2$ not only penalizes the Euclidean norm of Δz but regularizes the inversion of the composite linear operator that maps input perturbations to activation changes. Without it, the least-squares system could be ill-posed: small perturbations in the data or in the Jacobians would produce large, unstable changes in Δz . The regularizer acts as a spectral filter on the singular values of the operator.

If we stack the preservation and attraction terms into a single least-squares system,

$$E(\Delta z) = \|M\Delta z - y\|^2 + \lambda\|\Delta z\|^2, \quad M = \begin{bmatrix} \sqrt{1 - \gamma} A_S \\ \sqrt{\gamma} B_T \end{bmatrix}, \quad y = \begin{bmatrix} 0 \\ \sqrt{\gamma} b \end{bmatrix},$$

the normal equations read $(M^\top M + \lambda I)\Delta z = M^\top y$, yielding the closed-form solution

$$\Delta z^* = (M^\top M + \lambda I)^{-1} M^\top y.$$

Let $M = U\Sigma V^\top$ be the singular-value decomposition (SVD) of M , with orthogonal matrices $U \in \mathbb{R}^{p \times p}$, $V \in \mathbb{R}^{D \times D}$, and diagonal $\Sigma = \text{diag}(\sigma_1, \dots, \sigma_r)$ containing the non-negative singular values σ_k of M . Then $M^\top M = V\Sigma^\top \Sigma V^\top = V \text{diag}(\sigma_k^2) V^\top$, and substituting this expression into the normal equations gives

$$(V(\Sigma^\top \Sigma + \lambda I)V^\top)\Delta z = V\Sigma^\top U^\top y.$$

Multiplying on the left by V^\top (since V is orthogonal) and defining $\tilde{z} = V^\top \Delta z$ decouples the system into scalar equations $(\sigma_k^2 + \lambda)\tilde{z}_k = \sigma_k \langle u_k^\top, y \rangle$. Solving for each component yields

$$\tilde{z}_k = \frac{\sigma_k}{\sigma_k^2 + \lambda} \langle y, u_k \rangle, \quad \Delta z^* = V\tilde{z} = \sum_k \frac{\sigma_k}{\sigma_k^2 + \lambda} \langle y, u_k \rangle v_k.$$

Each triplet (u_k, v_k, σ_k) corresponds to a singular mode of the linear operator M : the vector v_k is a direction in input space, u_k its corresponding direction in activation space, and σ_k measures the sensitivity of activations to perturbations along v_k . The factor $\sigma_k/(\sigma_k^2 + \lambda)$ is the *Tikhonov filter factor*, which controls how much each mode contributes to the final update. For well-conditioned directions with $\sigma_k^2 \gg \lambda$, this factor approaches $1/\sigma_k$, so those modes are effectively inverted. For ill-conditioned directions with $\sigma_k^2 \ll \lambda$, the factor shrinks to σ_k/λ , strongly suppressing unstable components. Hence the Tikhonov regularizer acts as a *spectral low-pass filter* on the Jacobian operator M : it preserves well-supported modes and damps those that correspond to redundant or noisy directions in the activation geometry. Geometrically, the regularizer enforces smoothness by limiting the amplitude of Δz in directions where the mapping from input to activation is uncertain or degenerate. This explains why the Tikhonov formulation yields numerically stable and geometrically smooth perturbations, in contrast to the unregularized least-squares inverse that would amplify small singular values and produce erratic updates. In the context of MUSIC, this spectral filtering plays a crucial role: since the Jacobians of SOM activations are often highly correlated, some input directions change many activations in a similar way, producing nearly singular modes. The Tikhonov filter suppresses these ill-conditioned modes, ensuring that the resulting perturbation Δz^* follows a coherent and stable trajectory in the latent space. In summary, the decomposition

$$\Delta z^* = \sum_k \frac{\sigma_k}{\sigma_k^2 + \lambda} \langle y, u_k \rangle v_k$$

shows that Tikhonov regularization is not merely an L_2 penalty but an explicit spectral smoothing mechanism that stabilizes the inversion of the activation Jacobian and governs the smoothness of the induced dynamics in MUSIC.

The multiplicative factor $\sigma_k/(\sigma_k^2 + \lambda)$ attenuates components associated with small singular values, suppressing noisy or high-frequency directions in the null space of M . This mechanism is the hallmark of Tikhonov regularization and explains why it produces smoother, numerically stable perturbations compared to an unregularized least-squares inverse. The operator H inherits strong convexity from the λI term, which bounds its condition number $\kappa(H) \leq \|H\|/\lambda$. As a consequence, the solution satisfies $\|\Delta z^*\| \leq \lambda^{-1}\|r\|$, and its sensitivity to data perturbations is bounded by $\|\delta \Delta z\| \leq \lambda^{-1}\|\delta r\| + O(\kappa(H)\|\delta H\|)$. The parameter λ therefore tunes the bias-variance tradeoff: increasing it improves numerical stability at the cost of smaller update amplitudes, while decreasing it recovers the least-squares solution but may amplify noise.

S5 Probabilistic interpretation

From a probabilistic viewpoint, the quadratic energy E_γ can be interpreted as the negative log-posterior of a Gaussian Bayesian model that links input perturbations Δz to desired activation changes b . The relation between the two is modeled as a noisy linear observation process

$$B_T \Delta z = b + \varepsilon, \quad \varepsilon \sim \mathcal{N}(0, \sigma^2 I),$$

where ε represents random uncertainty or measurement noise in the target activation constraints. This defines the likelihood

$$p(b | \Delta z) \propto \exp\left[-\frac{1}{2\sigma^2} \|B_T \Delta z - b\|^2\right].$$

To regularize this inverse problem, we introduce a Gaussian prior on the perturbation itself,

$$p(\Delta z) \propto \exp\left[-\frac{1}{2\tau^2} \|\Delta z\|^2\right],$$

which encodes the assumption that, a priori, large deviations in input space are unlikely and that updates should remain close to the origin (or to the current z). The posterior over Δz given the observed activation change b is then

$$p(\Delta z | b) \propto p(b | \Delta z) p(\Delta z) \propto \exp\left[-\frac{1}{2} \left(\frac{1}{\sigma^2} \|B_T \Delta z - b\|^2 + \frac{1}{\tau^2} \|\Delta z\|^2\right)\right].$$

Maximizing this posterior (MAP estimation) is equivalent to minimizing its negative log, yielding

$$\Delta z^* = \arg \min_{\Delta z} \left(\frac{1}{\sigma^2} \|B_T \Delta z - b\|^2 + \frac{1}{\tau^2} \|\Delta z\|^2 \right),$$

which is precisely the Tikhonov–regularized least–squares problem with $\lambda = \sigma^2/\tau^2$. In this probabilistic reading, the regularization parameter λ is no longer arbitrary but acquires a clear meaning as the ratio between the noise variance in the measurement model and the prior variance of admissible perturbations. Large λ corresponds to strong confidence in the prior (small τ^2), producing conservative, small–amplitude updates; small λ corresponds to a permissive prior or highly reliable observations, allowing larger, more reactive updates.

The same reasoning extends naturally to the full MUSIC formulation, where both preservation and attraction terms appear as Gaussian likelihood components with distinct noise levels. If we denote $\varepsilon_S \sim \mathcal{N}(0, \sigma_S^2 I)$ and $\varepsilon_T \sim \mathcal{N}(0, \sigma_T^2 I)$ as independent noise sources for the two constraint sets, the joint likelihood reads

$$p(y | \Delta z) \propto \exp \left[-\frac{1}{2} \left(\frac{1}{\sigma_S^2} \|A_S \Delta z\|^2 + \frac{1}{\sigma_T^2} \|B_T \Delta z - b\|^2 \right) \right].$$

By identifying $\gamma = \frac{\sigma_S^{-2}}{\sigma_S^{-2} + \sigma_T^{-2}}$ and $\lambda = (\sigma^2/\tau^2)$ with appropriate scaling, one recovers the composite quadratic energy $E_\gamma(\Delta z)$ of Eq. (1). This shows that MUSIC can be understood as a *Bayesian inverse problem* in which the tradeoff between preservation and attraction is governed by the relative noise levels of the two constraint channels, while the Tikhonov term plays the role of a Gaussian prior on smoothness and amplitude of Δz .

This interpretation places MUSIC within the broader family of probabilistic inference frameworks that include ridge regression, Kalman filtering, and variational inference in Gaussian latent–variable models. In each of these, the solution represents a balance between data fidelity (likelihood) and regularity (prior), leading to minimum–variance linear estimators under Gaussian assumptions. Here, the same principle governs the flow of information between activation space and input space: the Tikhonov term ensures that the inverse mapping from activation changes to input perturbations is statistically well–posed, with λ acting as an interpretable signal–to–noise control parameter. Consequently, MUSIC admits a principled probabilistic foundation that connects geometric regularization with Bayesian inference, providing an additional theoretical justification for its stability and smoothness properties.

S6 Role of the row normalization

Row normalization of A_S and B_T is crucial to make γ an interpretable balance parameter: without normalization, differences in the scales of the Jacobian rows would bias the optimization toward either preservation or attraction independently of γ . Normalization equalizes the energy contribution of each prototype, ensuring that γ consistently weights the two objectives. The explicit form of Δz^* also reveals the close connection with the so–called Tikhonov projector used for partial preservation. When only the preservation constraint is considered, minimizing $\|A_S \Delta z\|^2 + \mu \|\Delta z\|^2$ yields the linear operator $P_\mu = I - A_S^\top (A_S A_S^\top + \mu I)^{-1} A_S$, which projects any direction onto the approximate null space of A_S , smoothly suppressing components that would change the preserved activations. The MUSIC update generalizes this idea by combining the projector–like preservation with the attraction term, both modulated by γ , under a single regularized inverse. In the limit $\lambda \rightarrow 0$, if the combined Jacobian $(1 - \gamma) A_S^\top A_S + \gamma B_T^\top B_T$ is full rank, the update converges to the exact least–squares solution; if it is rank–deficient, the Tikhonov regularizer selects the minimum–norm solution within the set of least–squares minimizers. For $\lambda \rightarrow \infty$, the update tends to zero, corresponding to complete damping. The limiting cases $\gamma = 0$ and $\gamma = 1$ represent pure preservation and pure attraction, respectively. Each MUSIC step can thus be interpreted as a regularized inverse mapping that converts infinitesimal activation changes into a stable and minimal–energy input displacement.

S7 Free-evolution trajectories under manifold-aware and unconstrained updates

To further analyze the qualitative behaviour of MUSIC, we design a free-evolution task where the system is not given any objective other than repeatedly applying random local perturbations in activation space.

Starting from the latent representation $z^{(0)}$ of an input face, at each step t we randomly select a prototype w_{j_t} and sample a random perturbation of its squared distance. In the MUSIC condition, this perturbation defines a linearized target constraint $B_T \Delta z \approx \delta$, while a small preservation set S (four nearest prototypes) constrains the update to remain consistent with the local SOM geometry. We compute the MUSIC direction d_{MUSIC} from the Tikhonov system $(M^\top M + \lambda I) \Delta z = M^\top y$ and apply a normalized step $\Delta z^{(t)} = \eta d_{\text{MUSIC}} / \|d_{\text{MUSIC}}\|$.

In the no-constraints baseline, the update direction is simply the radial vector $(z^{(t)} - w_{j_t}) / \|z^{(t)} - w_{j_t}\|$, again rescaled to the same step length η . Thus, the two trajectories differ only in their *direction*, not in their magnitude.

Despite identical step sizes, the two evolutions diverge sharply: unconstrained updates rapidly push the latent representation into regions that no longer decode into realistic faces, producing severe geometric distortions. Conversely, MUSIC maintains consistency with the local SOM geometry and evolves the face smoothly along semantically meaningful variations. Figure 11 displays a typical outcome.

S8 Algorithm pseudo-code for MUSIC exploration modes

This section provides step-by-step pseudo-code for the three MUSIC exploration modes defined in Section 4, including noise injection for enhanced coverage.

Noise injection. To enhance coverage and avoid premature alignment to local geometric modes, we inject small, controlled noise at three points: (i) *step noise* in input space, adding $\xi_z \sim \mathcal{N}(0, \sigma_z^2 I)$ to the deterministic update Δz before trust-region clipping; (ii) *target noise* on the right-hand side, perturbing the desired changes as $b \leftarrow b + \xi_b$ with $\xi_b \sim \mathcal{N}(0, \sigma_b^2 I)$; and (iii) *gradient jitter* by slightly perturbing the normalized Jacobian rows $\widehat{J}_j \leftarrow \widehat{J}_j + \Xi_j$ with small Frobenius norm $\|\Xi_j\|_F$. All noises are clipped by the trust radius to preserve local validity. In the cluster regime, *random target sub-sampling* $T^{(i)} \subseteq T$ at each relinearization pass further promotes diversity.

Table S1: Free exploration with geometry preservation and input-space step noise.

-
- Input:** prototypes $\{w_j\}_{j=1}^N$, current point z , weights W_S , ridge λ , trust radius τ , step-noise scale $\sigma_z \geq 0$.
Output: updated input z' .
1. Build $A_S = \text{stack}\{2(z - w_j)^\top : j = 1, \dots, N\}$ and form $C = (W_S A_S)^\top (W_S A_S) + \lambda I$.
 2. Compute smallest-eigenvector q_{\min} of C .
 3. Deterministic step: $\Delta z_{\text{det}} = \tau q_{\min}$ (or any vector in the low-eigenvalue subspace).
 4. Sample noise: $\xi_z \sim \mathcal{N}(0, \sigma_z^2 I)$ and clip $\xi_z \leftarrow \min\{1, \tau/\|\xi_z\|\} \xi_z$.
 5. Combine and clip: $\Delta z = \Delta z_{\text{det}} + \xi_z$, then $\Delta z \leftarrow \min\{1, \tau/\|\Delta z\|\} \Delta z$.
 6. Update $z' = z + \Delta z$ and relinearize at z' .
-

Table S2: Informed exploration (single target t) with target-noise and step-noise.

-
- Input:** prototypes $\{w_j\}$, current z , target t , weights W_S, W_T , penalties γ, λ , trust τ , fraction η , noise scales $\sigma_b, \sigma_z \geq 0$.
Output: updated input z' .
1. Set $T = \{t\}$, $S = \{1, \dots, N\} \setminus T$.
 2. Build A_S, B_T from normalized Jacobians $\widehat{J}_j = 2(z - w_j)^\top / \|z - w_j\|$.
 3. Desired change (squared distance): $b = -\eta a_t(z)$; add target-noise $b \leftarrow b + \xi_b$, $\xi_b \sim \mathcal{N}(0, \sigma_b^2)$.
 4. Solve normal equations:
$$[(W_S A_S)^\top (W_S A_S) + \gamma (W_T B_T)^\top (W_T B_T) + \lambda I] \Delta z_{\text{det}} = \gamma (W_T B_T)^\top (W_T b).$$
 5. Sample step-noise $\xi_z \sim \mathcal{N}(0, \sigma_z^2 I)$; set $\Delta z = \Delta z_{\text{det}} + \xi_z$.
 6. Trust region: if $\|\Delta z\| > \tau$, rescale $\Delta z \leftarrow \tau \Delta z / \|\Delta z\|$.
 7. Update $z' = z + \Delta z$; relinearize and optionally repeat (1–3 passes).
-

Table S3: Cluster exploration (multi-target): random target sub-sampling, single-prototype randomization, and noise-augmented updates.

Input: prototypes $\{w_j\}$, current z , full target set T , non-targets S , weights W_T, W_S , penalties γ, λ , trust τ , passes m , fraction η , sub-sampling rule (size k or keep-prob p), optional single-prototype flag, noise scales $\sigma_b, \sigma_z \geq 0$.

Output: updated input z' .

1. Initialize $z^{(0)} \leftarrow z$.
2. For $i = 0, \dots, m - 1$:
 - a. *Random target selection:*
 - **Multi-target sub-sampling:** draw $T^{(i)} \subseteq T$ either by fixed size $|T^{(i)}| = k$ or Bernoulli keep-probability p .
 - **Single-prototype randomization (optional):** draw a single target $t^{(i)} \sim \text{Uniform}(T)$ and set $T^{(i)} = \{t^{(i)}\}$.
 - b. Build $A_S^{(i)}, B_{T^{(i)}}^{(i)}$ from local Jacobians at $z^{(i)}$; apply weights W_S, W_T .
 - c. Desired target changes: $b_t^{(i)} = -\eta a_t(z^{(i)})$ for $t \in T^{(i)}$; add $\xi_b^{(i)} \sim \mathcal{N}(0, \sigma_b^2 I)$: $b^{(i)} \leftarrow b^{(i)} + \xi_b^{(i)}$.
 - d. Solve $(A_w^\top A_w + B_w^\top B_w + \lambda I) \Delta z_{\text{det}}^{(i)} = B_w^\top b_w$, with $A_w = W_S^{1/2} A_S^{(i)}$, $B_w = \sqrt{\gamma} W_T^{1/2} B_{T^{(i)}}^{(i)}$, $b_w = \sqrt{\gamma} W_T^{1/2} b^{(i)}$.
 - e. Sample step-noise $\xi_z^{(i)} \sim \mathcal{N}(0, \sigma_z^2 I)$ and set $\Delta z^{(i)} = \Delta z_{\text{det}}^{(i)} + \xi_z^{(i)}$.
 - f. Trust region: $\Delta z^{(i)} \leftarrow \min\{1, \tau / \|\Delta z^{(i)}\|\} \Delta z^{(i)}$.
 - g. Update and relinearize: $z^{(i+1)} = z^{(i)} + \Delta z^{(i)}$.
3. Return $z' = z^{(m)}$.
